ANNUAL REVIEWS

Annual Review of Biomedical Engineering

Biomedical Applications of Metal 3D Printing

Luis Fernando Velásquez-García[1] and Yosef Kornbluth[2]

[1]Microsystems Technology Laboratories, Massachusetts Institute of Technology, Cambridge, Massachusetts 02139, USA; email: Velasquez@alum.mit.edu

[2]Department of Mechanical Engineering, Massachusetts Institute of Technology, Cambridge, Massachusetts 02139, USA

Annu. Rev. Biomed. Eng. 2021. 23:307–38

The *Annual Review of Biomedical Engineering* is online at bioeng.annualreviews.org

https://doi.org/10.1146/annurev-bioeng-082020-032402

Keywords

biomedical instrumentation, directed energy deposition, biocompatible metal implants, biodegradable metal implants, metal 3D printing, powder bed fusion

Abstract

Additive manufacturing's attributes include print customization, low per-unit cost for small- to mid-batch production, seamless interfacing with mainstream medical 3D imaging techniques, and feasibility to create free-form objects in materials that are biocompatible and biodegradable. Consequently, additive manufacturing is apposite for a wide range of biomedical applications including custom biocompatible implants that mimic the mechanical response of bone, biodegradable scaffolds with engineered degradation rate, medical surgical tools, and biomedical instrumentation. This review surveys the materials, 3D printing methods and technologies, and biomedical applications of metal 3D printing, providing a historical perspective while focusing on the state of the art. It then identifies a number of exciting directions of future growth: (*a*) the improvement of mainstream additive manufacturing methods and associated feedstock; (*b*) the exploration of mature, less utilized metal 3D printing techniques; (*c*) the optimization of additively manufactured load-bearing structures via artificial intelligence; and (*d*) the creation of monolithic, multimaterial, finely featured, multifunctional implants.

Contents

1. INTRODUCTION

Today's world, with ubiquitous transportation, housing, food, and entertainment, is largely affordable due to the mass production of uniform designs via large-batch fabrication methods (1). However, these techniques are at odds with many biomedical applications in which using a base design is not feasible or practical, for example, to satisfy one-of-a-kind users; instead, these biomedical applications require customization and very different manufacturing technologies. In some of these applications, using metal is essential to attain satisfactory functionality and durability.

The biomedical applications of metals primarily focus on implants. Many metals and metal alloys are known (2), but only a few are safe to implant into people. Although metals have been used in medicine since antiquity, metallic implants were largely unsuccessful until the introduction of the aseptic surgical technique in the 1860s (3). Decades later, advances in materials science, such as vacuum processing, facilitated the use of metal alloys in implants (4). In the 1920s, stainless steel (SS) 316 was developed, with high resistance to corrosion by bodily fluids and other features of biomedical interest (5). In the 1930s, cobalt-chromium (Co-Cr) alloys, originally developed for the aerospace industry, were first used in medical implants (6); these alloys have better biocompatibility, corrosion resistance, and wear resistance than SS 316 (7). Pure titanium implants were introduced in the mid-1950s, followed decades later by Ti alloys with superior mechanical characteristics. Currently, Co-Cr and Ti alloys are the most common metals in orthopedics, with

SS 316 and SS 316L (a more ductile and corrosion-resistant, low-carbon version of SS 316) and nitinol (a shape-memory nickel-titanium alloy) having niche uses.

Presently, metals are used in a wide range of biomedical applications besides implants, including heart stents and valves, dentistry, surgical tools, scaffolds, and in vitro medical devices. With the aging of the world's population, advanced metals have enabled high-quality prosthetics that address bone fracture and tissue loss (7). The elderly population has greatly increased in the United States (from 4.9 million in 2002 to 39.7 million in 2010), and many younger people also have degenerative diseases, such as osteoarthritis and osteoporosis, and traumatic injuries, leading to pain or loss of tissue function (8). By 2030, hip replacements are expected to increase by 174% (i.e., 0.57 million procedures) and knee arthroplasties by 673% (3.48 million procedures) compared with 2000 (9).

Additive manufacturing (AM): process of joining materials to make objects from 3D model data, usually layer upon layer

Additive manufacturing (AM) is the process of joining materials to make parts, usually layer by layer, in contrast to traditional subtractive manufacturing, which selectively removes material from bulk, and formative manufacturing, which shapes bulk via pressure (10). AM makes possible the low-cost, small- to mid-batch production of customized, complex, monolithic, multimaterial parts (11). AM can use data from mainstream 3D medical imaging methods, for example, X-ray computed tomography (CT) and magnetic resonance imaging, directly in its manufacturing models. Personalized medical implants lower operation and hospitalization times, reducing overall medical costs, for both humans (12) and animals (13).

A key advantage of AM over traditional fabrication methods is its multiscale nature; geometries are defined using volume elements (voxels) that are generally many orders of magnitude smaller than the object's volume, enabling miniaturized and/or finely featured structures. In particular, a wide variety of microfluidics of biomedical interest have been reported (14, 15)—even complex, monolithic, multimaterial devices such as pumps (16, 17) and nanosatellite thrusters (18). Moreover, conceptually, the use of discretized volumes with associated physical properties to fully specify an object makes AM more repeatable (19).

This review covers the materials, printing methods, and biomedical applications of metal AM, providing a historical perspective, a focus on the state of the art, and a window to exciting directions of future growth.

2. PRINTABLE BIOMEDICAL METALS

This section summarizes the metallic materials most commonly used in biomedical applications: titanium, titanium alloys, Co-Cr alloys, SS, tantalum, gold, magnesium, gallium alloys, and iron (**Table 1**); each material can be processed via one or more AM methods (see Section 3).

The most common biomedical use of metal is orthopedic implants, and the different material options available result from addressing changes in clinical requirements (24). Some uses require inertness (e.g., Co-Cr alloys, gold); some require bonding with the host tissue (e.g., titanium, titanium alloys); and some require tissue growth and subsequent taking over of the implant (e.g., magnesium alloys, iron). Most modern implants use Co-Cr and Ti alloys (12, 24). An implantable metal must have biocompatibility, corrosion resistance, high specific strength (i.e., it must maximize mechanical resistance while minimizing weight), high endurance strength (maximum alternating stress that the material can experience without fatigue failure for a given number of cycles), high impact toughness (the material's ability to absorb energy via permanent deformation without fracturing), and low toxicity. A key issue with implants is stress shielding—that is, osteopenia due to stress suppression in the bone by the implant. Stress shielding can be addressed either by using a material with stiffness close to that of cortical bone (e.g., magnesium) or by engineering a porosity that reduces the implant's stiffness.

Table 1 Metals used in biomedical applications

Material	E (GPa)	σ_{US} (MPa)	ε_{MAX} (%)	ρ (g/cm^3)	Uses	References
Cortical bone	13.6–23.8	68–156	1.1–3.1	1.73–2.10	Natural skeleton	22, 34, 35
CP-Ti	105	240–550	15–24	4.54	Pacemaker cases, housings for ventricular-assist devices, implantable infusion drug pumps, dental implants, maxillofacial and craniofacial implants, screws and staples for spinal surgery	27, 31
Ti-64	110–114	895–930	6–10	4.20–4.50	Load-bearing implants	27, 31
Co-Cr	220–250	600–2,280	8–28	8.27–9.20	Load-bearing implants, fracture fixation devices	20, 21, 24
SS 316L	189–205	490–1,731	12–52	7.90–8.10	Short-term implants, hip stems, cannulae, dental impression trays, hypodermic needles, steam sterilizers, filters	22, 24, 26
Ta	186–191	205–480	1–30	16.69	Vascular clips, radiographic bone markers, nerve repair, cranial-defect repair, grafts/scaffolds, hip and knees, wires for skin closure, staples for abdominal surgery, electrical capacitors	23, 24
Au	80	130–200	4–50	19.30	Dental implants and fillings, wire fixings and supports, ocular prosthetics, endovascular stents, soluble injectable compounds to alleviate rheumatoid arthritis, drug delivery via nanoparticles	46, 51
Mg alloys	10–45	90–280	3–30	1.74–2.00	Biodegradable implants, tissue engineering	12, 22–24
Ga alloys[a]	NA	NA	NA	5.91–6.36	Flexible electronics, injectable electrodes, nerve repair	56
Fe alloys	188–215	357–412	9–15	7.48–7.87	Biodegradable implants, tissue engineering	12, 63

[a]Ga and its alloys are liquid above 29.8°C.

Abbreviations: E, Young's modulus; ε_{MAX}, maximum elongation; NA, not available; σ_{US}, ultimate strength; ρ, mass density.

2.1. Titanium and Its Alloys

Titanium and its alloys have been widely used in biomedical implants since the 1970s due to their excellent biocompatibility, good corrosion resistance, and high specific strength. Titanium has a hexagonal, close-packed lattice structure at room temperature, called α phase, and a body-centered cubic structure at 883°C, called β phase. Alloying elements such as Al, C, and O extend the α phase by increasing the β/α transus temperature, while Mo, Ta, and Nb extend the β phase by reducing the transus temperature (25). Consequently, Ti alloys can be classified into four main groups: α-, near-α-, (α + β)-, and β-type alloys. The mechanical properties of Ti alloys are strongly influenced by their composition, with the noticeable exception of the Young's modulus, which remains near constant (26). The most common Ti-based materials used today in biomedical applications

are commercially pure titanium (CP-Ti) and titanium alloy Ti6Al4V (Ti-64). CP-Ti (98.9% to 99.6% Ti alloyed with O and Fe) is a relatively weak α-type alloy that cannot be strengthened via heat treatment; consequently, CP-Ti is used in non-load-bearing, corrosion-resistant applications, such as pacemaker cases, infusion drug pumps, and dental implants (24, 27). In contrast, Ti-64 is an (α + β)-type alloy whose mechanical strength can be increased up to 50% via heat treatment without significantly affecting its Young's modulus (24), making Ti-64 compatible with load-bearing applications, such as fracture fixation plates, hip stems, fasteners, wires, and screws. Ti-64 extra low interstitials (ELI) alloy has fewer interstitial impurities such as O, N, C, and Fe, resulting in improved ductility and fracture toughness with some reduction in strength (28); consequently, Ti-64 ELI alloy has been widely used for bone fixation plates and in stems of artificial hip joints (29). The grain size of Ti alloys can be modified via plastic deformation; smaller grains have fewer atoms per grain and higher surface energy, promoting higher osseointegration. In particular, ultrafine-grained (grain structure in the submicrometer to nanometer range) CP-Ti and Ti-64 alloys have shown significantly better vascular and bone cell adhesion compared with conventional Ti-64 varieties (30). CP-Ti and Ti-64 spontaneously form a passive TiO_2 film that contains OH^- ions that react with the bones' mineral constituents, promoting osteointegration (31). Although 50% of biomedical implants use Ti-64 (31), the alloy causes some concern as it contains Al and V, which are cytotoxic; consequently, aluminum- and vanadium-free Ti alloys have been developed for implant applications (32). Furthermore, CP-Ti and Ti-64 are much stiffer than human bone, causing stress shielding. However, a key benefit of 3D-printed Ti-based materials is the inclusion, without resorting to chemical processes, of an engineered porous structure to match the stiffness of the implant with that of the natural bone; the porosity also enhances bone cell growth, creating a strong twist lock between the bone and the implant that improves the success rate of the implant (33–35). Titanium has also been shown to be more biocompatible than SS 316L (36).

2.2. Cobalt-Chromium Alloys

Co-Cr alloys have been used in medical implants since the 1930s (6). Co-Cr alloys are over an order of magnitude more corrosion resistant and have higher wear resistance than SS. The chromium forms a protective Cr_2O_3 film when exposed to the human body environment, causing excellent biocompatibility. Co-Cr alloys are often used in permanent, load-bearing implants, both medical and dental. 3D-printed dental implants made in Co-Cr alloy accurately mimic the structure of the alveolar bone (37). Moreover, Co-Cr is preferred over gold for dental implants due to its lower cost, better mechanical properties, and ability to maintain adequate bond strength when joined to the porcelain used for tooth surfaces. However, the longevity of Co-Cr prosthodontics is still not fully known (38).

Cobalt is an essential trace element, principally found in the maturation of human red blood cells as a constituent of vitamin B_{12}; however, it is toxic at high concentrations. Co-Cr implants release metallic particles, which in some patients can cause severe damage to nearby tissue (24). In particular, Co-Cr-Mo implants with metal-on-metal bearings release cobalt and chromium ions into the blood (39). Furthermore, cobalt toxicity has been reported to cause adverse reactions in some patients with metal-on-metal hip prostheses 4–5 years after implantation (40). The addition of calcium phosphide to the prosthetic and the laser processing of the alloy can slow down the release process (41).

2.3. Stainless Steel

SS alloys are iron alloys with at least 11% chromium and some nickel. The mechanical properties of SS can be controlled via doping and heat treatment. SS alloys can be grouped into four families,

depending on their microstructure: martensitic, ferritic, austenitic, and austenitic plus ferritic (26). The great majority of biomedical applications use austenitic SS, most commonly SS 316L, because of its availability, low cost, ease of fabrication, and biocompatibility. As in Co-Cr alloys, chromium creates a protective thin oxide film on the surface of SS objects. The addition of nickel to SS results in an austenitic microstructure at room temperature; however, nickel is toxic, leading to serious health issues if released due to corrosion (42). The addition of alloying elements such as molybdenum slows down the corrosion rate of SS alloys. Alternatively, nickel can also be replaced with nitrogen, which, in addition to facilitating a room-temperature austenitic microstructure, increases the alloy mechanical strength.

However, SS is not truly stain proof—it reacts, albeit slowly. Consequently, SS 316L is not used in permanent implants, as they suffer corrosion pitting, corrosion fatigue, and stress corrosion cracking due to sustained contact with the body's interior. The wear resistance of SS 316L is also relatively poor, leading to debris around the implant. SS 316L is used widely in surgical instruments and in cost-effective, short-term (months to years) implants; furthermore, high-nitrogen, nickel-free SS is popular for stems in permanent hip prostheses; for example, SS stems are used in 70% of hip replacements in the United Kingdom (24).

2.4. Tantalum

Tantalum has been used in biomedical engineering since the 1940s. Tantalum has good chemical stability—it has approximately the same corrosion resistance of glass; moreover, tantalum has better biocompatibility and fatigue resistance than titanium and supports enhanced bone ingrowth (12). Tantalum generates a protective Ta_2O_5 layer, which makes implantable parts inert to bodily fluids (43). Tantalum is used in vascular clips, radiographic bone markers, nerve repair materials, cranial-defect repair materials, grafts and scaffolds, hip and knee implants, wires for skin closure, staples for abdominal surgery, and implantable electronics (12, 24). Tantalum capacitors are exceptionally reliable and thus are used in implantable medical electronics such as hearing aids, neurostimulators, insulin pumps, and cardioverter defibrillators. However, tantalum is very difficult to machine or melt, and it is also over fivefold more expensive than SS and Ti alloys, greatly limiting its use. Consequently, biomedical applications commonly use tantalum coatings instead of bulk tantalum; examples include Ta-coated titanium implants (44) and carbon foam skeletons (45).

2.5. Gold

Gold is widely used in engineering because of its excellent chemical resistance, high infrared reflectance, malleability, ductility, electrical conductivity, and heat conductivity. Gold is very expensive; consequently, electroplated goods are common. Elements such as copper, silver, platinum, palladium, and zinc are often added to gold to increase its strength. Gold has excellent resistance to shearing and pulling, making it suitable for dental crowns and bridges, while gold's ductility ensures a close fit between teeth and an implant (46). Thermal treatments change the microstructure of gold alloys—increasing its strength, for example. In addition, gold alloys wear at a rate similar to that of enamel, minimizing differential abrasion (47).

Gold is used in restorative dentistry for implants and fillings, gold wire fixings, and supports (48); in ocular prosthetics (49)—particularly for upper eyelid implant surgery (46); in endovascular stents (46); and as soluble injectable compounds to alleviate rheumatoid arthritis and to treat/prevent bacterial infections (50). Properly installed, gold dental implants last the longest (51). Gold nanoparticles exhibit different physical and chemical properties than bulk gold because their large surface-to-volume ratio makes them more reactive; consequently, a wide range of functionalized gold nanoparticles have been explored for therapeutic and diagnostic applications (52).

2.6. Magnesium and Its Alloys

Magnesium participates in many biochemical reactions, including energy metabolism and protein synthesis; in addition, magnesium helps regulate blood sugar and keep bones strong. Magnesium is absorbed by the digestive system and eventually filtered by the kidneys. In air, magnesium forms a protective oxide film; however, the film dissolves in the body's saline environment, making magnesium alloys, particularly Mg-Ca varieties (in which up to 0.8 wt% calcium is added to greatly improve magnesium's corrosion resistance), fully absorbable by the body (24). Consequently, magnesium alloys are biodegradable. Magnesium implants are temporary structures that promote native tissue growth, while the body absorbs them, until new tissue replaces the implant. In comparison, Ti, Co-Cr, and SS implants, which are not biodegradable, must be surgically removed or adjusted (12). Magnesium has excellent biomechanical compatibility with human bone; for example, their mass densities and Young's moduli are very similar (53), avoiding stress shielding. Magnesium also possesses unique osteopromotive properties—the release of Mg ions stimulates bone formation at the periosteal region (53).

Magnesium can also be alloyed with other elements to change its properties. For example, Mg-Mn alloys have improved corrosion resistance, Mn-Zn and Mn-Cu alloys have higher strength, and Mn-Al alloys have a good combination of mechanical properties and corrosion resistance (24). The use of magnesium alloys in implants poses several challenges, including infection and hydrogen bubble generation; the latter can be addressed by nucleating the magnesium alloy as a metallic glass, that is, an amorphous, single-phase structure (54). Magnesium is flammable and thus needs an inert/vacuum atmosphere to be 3D printed; Mg parts can also be created using printed scaffolds (55).

2.7. Gallium Alloys

Gallium and its alloys are biocompatible materials that are liquid near room temperature (56). Ga compounds are anti-inflammatory, antimicrobial, and immunosuppressive in animal models of human disease (57). Popular Ga alloys are Galinstan (gallium, indium, and tin) and eutectic gallium indium (EGaIn). Ga and its alloys have a melting temperature below 30°C, high electrical conductivity ($\sim 3.1 \times 10^6$ S/m), water-like viscosity, and more than 15 times the thermal conductivity of water (56, 58). In a Ga alloy, the Ga portion predominantly oxidizes, creating a protective layer that can be stripped with an acid or alkaline solution (59).

Ga alloys can satisfy many biomedical applications for which solid metals are unsuitable, including vascular embolization tumor therapy (56), nerve reconnection (60), and flexible interconnects (61). In addition, Ga alloy nanoparticles can be functionalized with a metal thiolate complex and thus used in drug-delivery applications (58). Ga alloys are also self-healing, which is useful in antennas and electrodes for biomedical applications. For example, when a channel filled with a Ga alloy is cut, the alloy generates a protective oxide at the cut that prevents the liquid metal from retreating into the channel or dripping outside; if the two parts are reconnected, the liquid metal eventually coalesces and electrical conduction is reestablished. If the channel is made of a self-healing polymer, the channel would also heal mechanically (62).

2.8. Iron

Iron is an essential trace element in almost all living organisms; in particular, iron is present in the proteins hemoglobin and myoglobin (required for transporting oxygen to the tissues) and in other metabolic enzymes and proteins (24). However, iron is toxic at high concentrations. Iron-based materials are a promising choice for biodegradable implants due to their excellent mechanical

properties and biodegradability given that iron ions released during degradation are metabolized and not accumulated (12). However, among biodegradable pure metals, iron has the highest yield strength and elastic modulus, much higher than those of cortical human bone (63); moreover, the degradation of pure iron in physiological media is slower than what would be required in the human body for a biodegradable implant (64). Consequently, research efforts have focused on developing porous structures made of iron and iron-based compounds instead of solid, pure iron to minimize stress shielding and to increase the degradation rate, with the aim of using the objects as temporary structures that promote native tissue growth (12). Fe alloys such as Fe-Mn, Fe-Mn-Ca, and Fe-Mn-Mg have been investigated for biodegradable implants; typical porosities fall between 35% and 53% (12, 63).

Electron-beam powder bed fusion (PBF-EB): AM method that uses loose fine powder and a rastering electron beam to create objects

Laser powder bed fusion (PBF-L): AM method that uses loose fine powder and a rastering laser beam to create objects

Direct metal laser sintering (DMLS): PBF-L method in which the laser sinters the loosened powder to create objects

Selective laser melting (SLM): PBF-L method in which the laser melts the loosened powder to create objects

3. METAL 3D PRINTING TECHNOLOGIES

Metal AM is at the intersection of information and metal processing technologies, bypassing many of the costs associated with traditional processes, equipment, and skills for metal working, while creating free-form, near-net-shape 3D objects (19). This section presents the AM methods according to how the printable material, that is, feedstock, is supplied to the integrating agent. Specifically, the metal AM techniques covered encompass (*a*) bulk-supplied powder feedstock selectively joined into a solid object using light, electrons, or binder and (*b*) liquid/paste, filament/wire, or powder feedstock directly fed to the integrating agent, that is, light, electrons, plasma, heat, or binder, to create a printed object. Metal AM often requires postprinting annealing to consolidate the print, transform the feedstock into metal, or nucleate a desired microstructure (19).

In AM, 3D-printed objects are discretized using voxels that are typically six or more orders of magnitude smaller than their volume; consequently, creating porous structures via AM is straightforward—provided the geometry of the printed object allows for the removal of any internal unprocessed feedstock. In particular, the effective stiffness of 3D-printed biomedical implants can be tailored to match that of the bones, avoiding stress shielding, while textured surfaces can also promote tissue growth (12, 24).

3.1. Metal Additive Manufacturing Methods with Bulk-Supplied Feedstock

Loose, fine metal powder feedstock can be selectively combined into an object using light, electrons, or droplets of binder as an integrating agent (19, 65). AM methods with bulk-supplied feedstock use more printable material than what is actually integrated into the object; however, the unprocessed powder can be recycled to a certain extent (66), reducing waste. Bulk-supplied feedstock AM methods generally create single-material objects.

3.1.1. Powder bed fusion. Powder bed fusion (PBF) is the most popular metal AM method with bulk-supplied feedstock. In PBF (**Figure 1*a***), a high-energy electron beam (for electron-beam PBF, known as PBF-EB) or a CO_2/Nd:YAG/diode laser (for laser PBF, known as PBF-L) rasters a bed of fine powder, selectively fusing it. As the powder bed is incrementally lowered, a fresh layer of powder is applied on top of the existing printed object via a blade or roller, while the beam selectively fuses portions of it to previously solidified layers (19). PBF-L is widely referred to in the literature as direct metal laser sintering (DMLS), selective laser melting (SLM), or selective laser sintering, depending on the degree of melting; PBF-EB is also known as electron-beam melting. The first PBF-L system processed powder feedstock via selective laser sintering and was invented by Carl Deckard in 1986 (67) and commercialized by DTM Corporation in 1992 (65). In

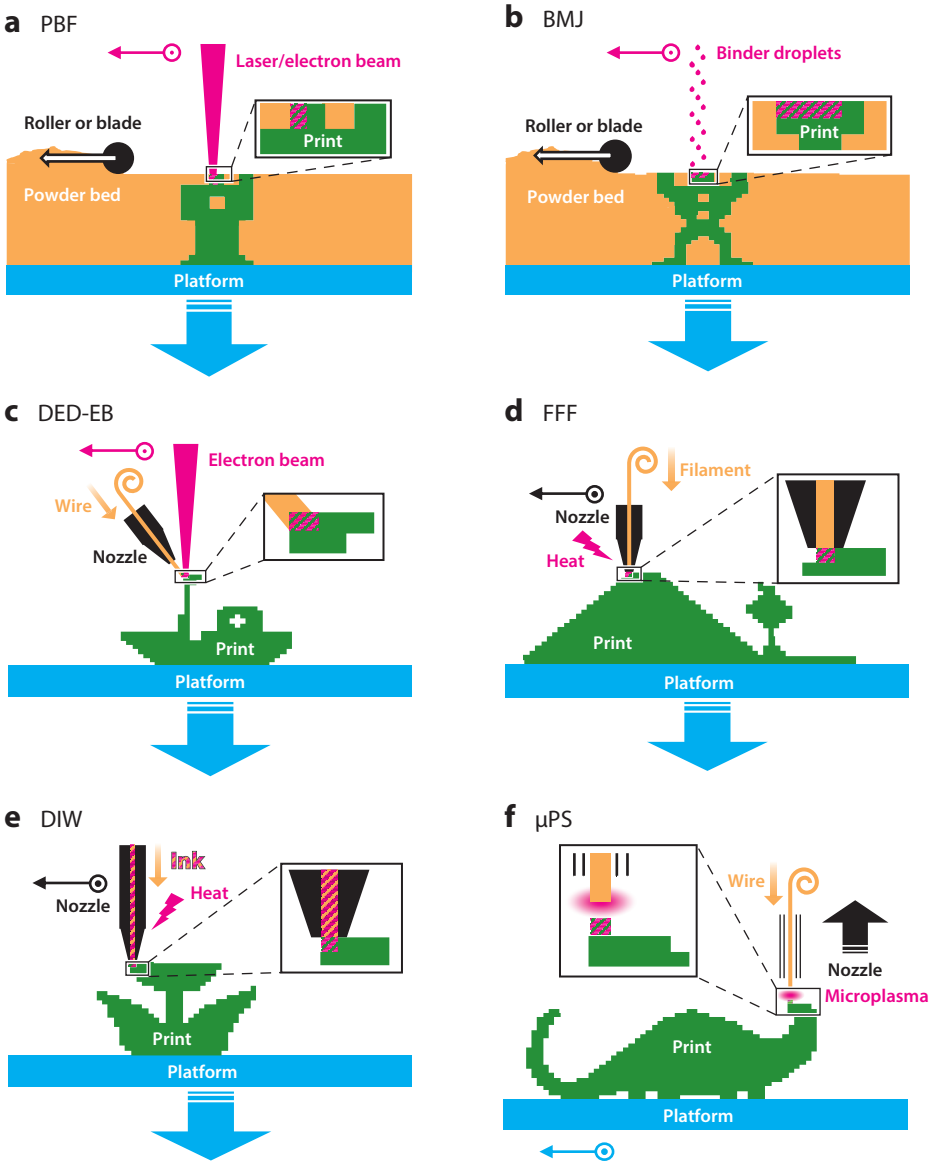

Figure 1

Schematics of selected metal additive manufacturing methods with bulk-supplied feedstock: (*a*) powder bed fusion (PBF) and (*b*) binder material jetting (BMJ). Schematics of selected metal additive manufacturing methods with feedstock directly supplied to the integrating agent: (*c*) electron-beam-directed energy deposition (DED-EB), (*d*) fused filament fabrication (FFF), (*e*) direct ink writing (DIW), and (*f*) microplasma sputtering (μPS).

1999, Fockele and Schwarze in cooperation with Fraunhofer ILT developed the first SLM systems (68). In 2001, the first DMLS printers to process 20-μm-tall layers were commercialized by EOS GmbH (65). Currently, DMLS systems have 100-W to 1-kW lasers, adequate to fully melt metal feedstock, and SLM and DMLS are used interchangeably (69).

The powder bed provides mechanical support to the printed object, often obviating the need to print supports for objects such as cantilevers, inclined walls, and domes. However, loose powder can remain in the internal cavities of a PBF-printed object without an adequate egress; consequently, PBF is generally unfit to create monolithic objects with high-aspect-ratio internal voids, such as microfluidics, even if the voids are not blind. A PBF-printed object can be reworked by removing the undesired portion, repositioning the resulting part in the printer platform using a customized fixture, and printing the remainder (19), which could be made of a different powder feedstock.

In a PBF-L system, a laser rasters each layer using a scan path of overlapping weld beads. The laser is rastered using magnetically driven mirrors, allowing for rapid movement of the beam. The laser penetrates deeper than the new layer to fuse it to previously printed layers. PBF-L systems can print metal parts with low porosity and can process many alloys of biomedical interest including stainless steel, titanium, Co-Cr, magnesium, and iron. The build speed, dimensional accuracy, printed mass density, and surface finish of PBF-L systems have greatly improved in the last decade, and they can now print near-net-shape objects (19).

In a PBF-L system, the build chamber is filled with inert gas to avoid the oxidation of the printed object. PBF-printed parts have an intricate thermal history due to sequential consolidation of feedstock in small segments and the partial remelting of the material in subsequent layer depositions, leading to significant accumulation of residual stresses (19, 65). Furthermore, PBF-fabricated parts usually exhibit mechanical anisotropy due to the directional microstructure generated during cooling (70), with the out-of-layer direction generally the weakest.

The microstructure and mechanical properties of PBF-L-printed objects are affected by laser energy density, platform temperature (71), layer thickness (72), hatch distance (73), and composition and pressure of the sintering atmosphere (74). The issues posed by the complex metallurgical conditions during PBF-L, including overlapping of melt pools, layer-by-layer stacking, and extreme temperature gradients, are unresolved and are being actively investigated (19). Recent improvements on PBF-L systems include feedstock heating to decrease the necessary laser heating, and thus increase processing speed, and purer gases to process reactive metals, such as magnesium.

Using an electron beam instead of a laser introduces key advantages, including (*a*) higher energy density for faster printing; (*b*) ultrahigh-vacuum operation for creating parts with more uniform temperature distribution, lower residual stresses, and less porosity and for printing highly reactive materials, such as magnesium; (*c*) reduction or elimination of support structures, making possible part stacking (e.g., hip cups) and decreasing secondary machining operation postprinting; and (*d*) creation of parts with less gradient in the microstructure for more consistent and uniform mechanical properties (75). Like their PBF-L counterparts, PBF-EB systems raster the electron beam across 3D space to melt the feedstock; however, the steering is done with electromagnetic coils instead of moving mirrors, greatly increasing the scan rate—up to 8,000 m/s (19). During printing, helium is leaked into the PBF-EB chamber to reduce the electrostatic charging of the powder and to cool the printed object. PBF-EB-printed objects require less support than those printed via PBF-L because the electron beam partially sinters the loose powder surrounding the object. The powder used in PBF-EB needs to be electrically conductive. In principle, this is not an issue for metal feedstock, although metal powders coated with oxide or nitride films could be challenging to print as they have significantly lower electrical conductivity compared with bulk metal; dielectrics are unsuitable for EB-based AM (76). PBF-EB systems tend to have higher deposition rates than their laser-based counterparts (19). In a PBF-EB system, the ultrahigh vacuum allows the preheating of the powder to 700°C, reducing the energy supplied by the electron beam to melt feedstock and reducing stress accumulation. The smallest reported spot size of PBF-EB is ∼100 μm (19). Arcam, a General Electric subsidiary and a major commercial vendor of PBF-EB systems, focuses

on titanium and Cr-Co alloys, which have biomedical importance. The wall-plug efficiency (conversion of electrical energy into a high-energy beam) of an EB-based AM system can be as high as 95%, while the wall-plug efficiency of a laser-based AM system oscillates between 20% (CO_2 laser, Nd:YAG laser) and 70% (diode laser) (76). Compared with their laser-based counterparts, PBF-EB systems have two key limitations: object cooling (hours to days) and a need for coarser powders (typical average powder diameter for PBF-L is 10 μm, while for PBF-EB it is 45 μm; see 19), which affect the surface finish and resolution; moreover, surface roughness concentrates stress, decreasing the mechanical strength of the printed part.

Binder material jetting (BMJ): AM process in which a liquid bonding agent is selectively deposited to join powder materials

The processing differences between PBF-L and PBF-EB result in printing parts with different properties when using the same feedstock. For example, Ti-64 printed via PBF-L exhibits an α martensitic microstructure, while printing the same material via PBF-EB shows a needle-like α + β Widmanstätten microstructure (77). Also, due to the nonuniform cooling, the porosity and residual stress of as-printed Ti-64 PBF-L-printed samples are larger than those of PBF-EB-printed samples; moreover, the mechanical properties of PBF-L-printed Ti-64 are anisotropic, in contrast to the isotropic mechanical properties of PBF-EB-printed Ti-64 (77).

3.1.2. Binder material jetting. Binder material jetting (BMJ) was developed by Sachs and Cima in 1993 and commercialized by ExOne (formerly Extrude Hone Corporation) in 1999 (19). Since the early 2010s, multiple companies, from start-ups to large, well-established companies, have also introduced BMJ tools to the market. BMJ is a two-step process that decouples the printing of the part from its sintering/consolidation. In the first step of BMJ (**Figure 1*b***), objects are created by injecting binder (a slurry of water and polymer) at room temperature into the regions of the powder layer that will be part of the object; during drying, water evaporates and the polymer coalesces the powder particles (72). Layers of powder are sequentially deposited via a roller or blade, as in PBF systems. After completing the first step, the printed object, immersed in loose powder, is heated to increase its mechanical strength. The printed objects are green, that is, they need to be debinded and sintered. The green part is extracted from the unprocessed powder and transferred to a specialized furnace to burn out the binder and sinter the object (78), with processing specifications dictated by the powder and binder composition. As in PBF systems, the unprocessed powder in a BMJ tool can be recycled. Because the sintering environment is homogenous, BMJ-printed parts have a uniform microstructure and show isotropic mechanical properties.

BMJ presents multiple advantages over PBF. In particular, (*a*) BMJ decouples the definition of the object from its sintering/solidification, eliminating stress buildup issues; (*b*) BMJ is more precise than PBF because of the gentler sintering and because the binder is supplied through an inkjet head with ∼35-μm pixels, rather than the ∼100-μm typical spot size of PBF systems; (*c*) BMJ machines are cheaper because the printhead doesn't need to deliver the high power of lasers or electron beams; and (*d*) BMJ systems are typically faster. However, porosity is a major concern with BMJ-printed parts, as this technique is, essentially, a powder metallurgy process (78). Porosity reduction is attained during sintering of the printed part; reducing the porosity in the printed material can significantly improve its mechanical properties as porosity acts as stress concentrator, promoting crack propagation (79).

BMJ uses a powder bed that, as described above, supports the printed parts, minimizing the need for support structures when printing free-form objects. Sun and colleagues characterized finely featured parts of interest in miniaturized systems (submillimeter details, with total dimensions on the order of a few centimeters or smaller) made with various commercial metal AM technologies (80). For PBF-L and BMJ of SS 316L, computer-aided design (CAD) and printed dimensions were highly linear; however, BMJ offered higher fidelity to the CAD dimensions, lower average in-layer offset (10 μm versus 100 μm), and lower average out-of-layer offset (25 μm

versus 100 μm). Nonetheless, the in-layer minimum feature size (the smallest positive features that could be resolved) was smaller using PBF-L than using BMJ (185 μm versus 285 μm).

The morphology and density of BMJ-printed parts are affected by powder size, layer thickness, binder concentration, packing density, and heat treatment (81). Finer powder increases the density of the part and improves resolution; thicker layers reduce the processing time but increase porosity. High binder concentration increases failure during binder burnout; however, low binder concentration reduces mechanical stability. Commercial BMJ systems can print metals of interest to biomedical applications such as SS 316L, Ti-64, Co-Cr, and CP-Ti (82); research-grade BMJ printing of magnesium (83) and Fe-based alloys (84) has been reported.

Laser-directed energy deposition (DED-L): AM process wherein a laser beam selectively fuses feedstock to partially printed objects by melting

Electron-beam-directed energy deposition (DED-EB): AM process wherein an electron beam selectively fuses feedstock to partially printed objects by melting

Laser-engineered net shaping (LENS): AM process wherein a laser beam selectively fuses feedstock by melting; also known as DED-L

3.2. Metal Additive Manufacturing Methods with Feedstock Directly Supplied to the Integrating Agent

There are metal AM methods that supply the feedstock directly to the integrating agent (light, electrons, heat, binder, or plasma). These methods address some of the shortcomings of the bulk-supplied feedstock methods discussed in Section 3.1. Specifically, (*a*) they can create monolithic, multimaterial/gradient material objects; (*b*) the printed parts are not immersed in unprocessed feedstock, minimizing the raw material needed to create an object; and (*c*) some of these methods can rework printed objects without a special fixture or part alignment (19).

3.2.1. Directed energy deposition. Directed energy deposition (DED) is the most common metal AM method with feedstock directly supplied to the integrating agent. DED systems combine a cladding system and a five-axis welder, and can use either a laser [via laser-directed energy deposition (DED-L)] or an electron beam [via electron-beam-directed energy deposition (DED-EB)] to integrate the feedstock to the printed part (65).

The use of electron beam welding and wire feedstock for AM was pioneered by Vivek Davé in 1995 (85), and Karen Taminger at NASA developed the process further and called it electron beam freeform fabrication; the patent of the process was filed in 2003 and issued in 2007 (86). In 1995, Sciaky, a supplier of welding systems, began research on AM using an electron beam and wire feedstock; in 2009, Sciaky made available as a service its DED-EB process, called electron beam direct manufacturing, and in 2014 it began commercializing systems based on the technology (**https://www.sciaky.com/about-us**). In 1995, Sandia National Laboratories developed a DED process that uses powder feedstock and a laser as an integrating agent, calling it laser-engineered net shaping (LENS); this technology was first commercialized in 1998 by Optomec (87). Other major vendors of DED-L systems include RPM Innovations and DM3D.

Similar to PBF-EB, DED-EB operates in vacuum and produces parts made of purer materials compared with parts created by DED-L. In DED-L systems, a wire can be directly fed to the integrating agent as feedstock, which is then melted to incorporate it into the partially printed object; however, powders are preferred as feedstock in DED-L systems because wire feedstock results in coarse, low-resolution parts that require labor-intensive postprocessing and because of the challenges of feeding the wire to a freely moving printhead (19). In contrast, DED-EB systems (**Figure 1*c***) use wire as feedstock because a powder jet is incompatible with the ultrahigh-vacuum environment of DED-EB. DED-printed products often have larger stress buildups than their PBF-printed counterparts because of the absence of a cooling medium such as loose powder (65); solutions for this issue include (*a*) design optimization, for example, avoiding large areas; (*b*) rotating the rastering direction layer by layer; and (*c*) thermal annealing postprinting (12). DED systems can print materials of biomedical interest, including titanium alloys, SS, and tantalum.

3.2.2. Fused filament fabrication. Fused filament fabrication (FFF), also called fused deposition modeling (FDM), was invented by Scott Crump in the late 1980s and commercialized by Stratasys in 1991 (65). In FFF, a hot nozzle extrudes thermoplastic filament, creating solid objects by rastering a shape layer by layer (**Figure 1*d***). Polymer FFF is widely popular due to the successful replicating rapid prototyper (RepRap) movement, founded by Adrian Bowyer in 2005 with the goal of creating low-cost 3D printing hardware that can manufacture many of its own components. BASF recently introduced the FFF-printable filament Ultrafuse® 316L (88)—composed of SS 316L microparticles (80% by weight) embedded in a binder matrix. The FFF-printed metal objects are green and require specialized furnaces for postprocessing the printed part. However, major filament vendors such as MatterHackers (**https://www.matterhackers.com**) have negotiated third-party services to do so, making metal AM available to anyone with an FFF printer capable of extruding feedstock at 230°C, as many commercial FFF printers can. At a more exploratory level, the start-up The Virtual Foundry (**https://www.thevirtualfoundry.com**) sells FFF-printable filaments made of various metals of interest to biomedical applications including tungsten (for X-ray shielding applications), SS 316L, and titanium; these filaments are made of metal microparticles embedded in Filamet™—a polylactic acid–like binder that can be extruded with a 235°C nozzle and removed via vacuum sintering. There are also reports of FFF-printed magnesium alloys (89), which are of great interest for biodegradable implants. The filament is made of Mg alloy AZ81 in powder form, mixed with organic binders; after printing and annealing in an argon atmosphere supplemented with getters, the material mimics the mechanical properties of human bone (90).

3.2.3. Direct ink writing. In direct ink writing (DIW), ink, that is, liquid/paste feedstock (a mix of solvent, binder, and filler), is extruded from a reservoir through a nozzle using pressure or a displacement as an actuation mechanism, with little or no heating of the feedstock (91). DIW creates objects in a similar manner as FFF, that is, by rastering the object layer by layer with a nozzle that extrudes feedstock (**Figure 1*e***). In a DIW system, if heat is needed to extrude the ink, it is typically supplied using a reservoir jacket with significantly less power density than what FFF extruders use to extrude their feedstock. Silver nanoparticle inks have produced metal microstructures with ~30% the electrical conductivity of bulk metal after laser sintering (92). Gold nanorod–based inks for cardiac constructs and other electrogenic tissues (93), and iron/ion oxide nanoparticle-based inks for bone regeneration, drug delivery, and hyperthermia (94), have been reported.

DIW inks can be metal clays—thick pastes of metal microparticles and a water-soluble organic binder; metal clays were invented in the 1990s for the jewelry industry and allow the creation of complex parts without requiring extensive training (95). The Mini Metal Maker (a modified FFF printer with a high-torque stepper motor to extrude metal clay) was developed and commercialized by David Hartkop in 2013; printed objects are desiccated and then annealed, producing solid, full-metal objects (96). Segura-Cárdenas and Velásquez-García recently used DIW to create microfluidics with silver clay as feedstock, demonstrating working, watertight closed channels as narrow as 200 μm and a catalytic microreactor that decomposes hydrogen peroxide for applications such as portable ejector pumping and sterilization (97).

3.2.4. Microplasma sputtering. Interconnects and other metal structures in commercial integrated circuits and microsystems are made via sputtering—the extraction of atoms from a solid via collision of energetic plasma ions (98). Sputtering is normally conducted in vacuum; however, plasmas can be stable at atmospheric pressure if the interelectrode distance is reduced to millimeters or less—these plasmas are called microplasmas. Microplasma sputtering (μPS) (**Figure 1*f***) is a relatively new technology for metal 3D printing of micro- and nanosystems that can deposit metal

Fused filament fabrication (FFF): AM method wherein a hot nozzle extrudes thermoplastic filament to create solid objects; also known as FDM

Fused deposition modeling (FDM): AM method wherein a hot nozzle extrudes thermoplastic filament to create solid objects; also known as FFF

Replicating rapid prototype (RepRap): open-source self-replicating rapid prototyping machine that uses FFF to make engineering components and other products from thermoplastics

Direct ink writing (DIW): AM method in which a fluid is extruded from a nozzle while rastering across a platform

Microplasma sputtering (μPS): AM method in which a low-current plasma at atmospheric pressure sputters a wire to direct-write traces on objects

Table 2 Summary of metal AM techniques for micro- and nanostructures

Metal AM technique	Electrical resistivity	Materials demonstrated	Minimum feature size (μm)	Substrate constraints	Postprocessing	References
DIW	3× bulk	Ag	2	NKC	Thermal/laser anneal	91, 92
EHDP	10× bulk	Au, Ag, Cu, W, Al	10	Conductive	Thermal anneal	92, 106, 107
LAED	100× bulk	Au	<1	Conductive	Thermal anneal	92, 109
LIFT	10× bulk	Al, Cu, Au, alloys	3	NKC	None	92, 110, 111
MCE	2× bulk	Cu, Pt, Ag	<1	Conductive	None	92, 112, 113
LIP	10× bulk	Ag, Cu, Au	1	Transparent	None	92, 114–116
FIBID	10× bulk	Al, Au, Fe, Co, Pt, W	<1	Conductive	Thermal anneal	92, 117, 118
μPS	1.2× bulk	Au, Cu	2	NKC	None	99–105, 119

Abbreviations: AM, additive manufacturing; DIW, direct ink writing; EHDP, electrohydrodynamic deposition printing; FIBID, focused-ion-beam-induced deposition; LAED, laser-assisted electrophoresis deposition; LIFT, laser-induced forward transfer; LIP, laser-induced photoreduction; MCE, meniscus-confined electroplating; μPS, microplasma sputtering; NKC, no known constraints.

at room temperature on a wide range of materials, including temperature-sensitive substrates (99–105). There is an experimental DED technique that uses an arc plasma as an integrating agent, known as plasma-arc directed energy deposition (DED-PA), but it produces large structures with low precision, resolution, and surface quality (19); instead, μPS uses a low-current glow discharge for finer process control. Because μPS does not use binder, it creates imprints with near-bulk electrical conductivity without annealing (~85% bulk value for gold), surpassing competing technologies such as electrohydrodynamic deposition (jetting of metal micro/nanoparticle solutions using high electric fields; see 106–108), laser-assisted electrophoretic deposition (creation of deposits via electrophoresis of metal micro- and nanoparticles confined by high-intensity photons; see 109), laser-induced forward transfer (direct transfer by laser ablation of materials sourced as a thin film on a transparent substrate; see 110, 111), meniscus-confined electroplating (see 112, 113), laser-induced photoreduction (photochemical reduction of metal salt solutions using a rastering laser; see 114–116), and focused-ion-beam-induced deposition (deposition of metallic molecules from the ion-induced dissociation of gases; see 117, 118) (**Table 2**). In principle, many materials can be sputtered, but the reported μPS work focuses on gold and copper (see 99–104). Because of the slow speed of the process, μPS is primarily used for metallic coatings, rather than metal objects, which can be used to integrate metal traces to the surfaces of free-form objects, for example, to implement skin electronics. Recent work on μPS using a high-speed coaxial flow reactor and gold feedstock has shown deposition rates on par with traditional (vacuum) sputtering and excellent film adhesion without employing an adhesion layer, annealing, or any other pre/postprocessing steps (119).

4. METAL 3D-PRINTED BIOMEDICAL APPLICATIONS

In this section, the progress on metal 3D-printed biomedical devices is surveyed, with a focus on the latest reports and the materials covered in Section 2. The literature is organized by the kind of development (permanent implants, biodegradable implants and scaffolds, surgical tools, and biomedical instrumentation), arranged within each group by the metal used. The great majority of reports focus on load-bearing prosthetic implants, as metals are traditionally used to replace

hard tissue. Prosthetic implants harness two key strengths of AM: customization, which reduces recovery time and intervention cost (12), and controlled porosity, which eliminates stress shielding (24). The great majority of 3D-printed prosthetics are made via PBF. AM in orthopedics was first proposed by Jamieson et al. in 1995 (120).

4.1. Permanent Implants

This section reports the latest developments on permanent 3D-printed metal biomedical implants; examples include dental, maxillofacial, craniofacial, load-bearing, sternocostal, and spine fusion implants and cardiovascular stents. In most cases, permanent implants take advantage of modern medical imaging techniques such as CT to closely match the patient's anatomy. The grain structure, porosity, and surface of the implant can be tailored to foster cell adhesion, minimize stress shielding, and control drug delivery. Materials used in permanent biomedical implants reported in this section include titanium alloys, Co-Cr alloys, tantalum, and gold—the latter is used as a nanocomposite to regenerate functional tissue.

4.1.1. Titanium alloys. 3D-printed Ti alloy prosthetics have been developed for dental (121), maxillofacial (121a), craniofacial (122), load-bearing (123), sternocostal (124), and spine fusion (125) implants. In 2015, Hsu & Ellington (126) reported excellent results one year after using a roughened, 3D-printed titanium cage truss to treat a tibial nonunion; later, Dekker et al. (127) reported an 87% clinical success rate in a follow-up study of 15 patients with customized 3D-printed Ti implant cages to address severe bone loss, deformity, and/or arthrodesis. In 2012, Murr and colleagues (128) reported porous Ti-64 PBF-EB-printed knee and hip implants (**Figure 2*a***), avoiding stress shielding and promoting bone growth. In 2020, Mangano et al. (129) reported a complication rate of 30% in 10 elderly patients with custom PBF-L-printed titanium mandible implants. Popov and colleagues (130) reported a Ti-64 PBF-EB-printed implant to reconnect a broken clavicular bone (**Figure 2*b***); the implant includes a monolithic lattice that promotes bone growth and mimics the inner structure of human bones—large voids with 55% to 70% interconnected porosity. Barbin et al. (131) investigated Ti-64 full-arch fixed dental prostheses made via

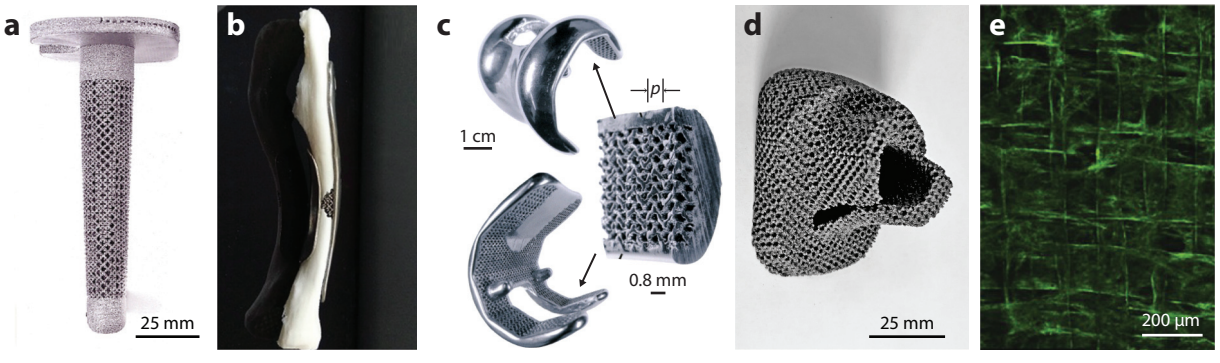

Figure 2

Examples of metal 3D-printed, permanent, nonbiodegradable implants. (*a*) Ti-64 tibial stem with monolithic mesh structure. Panel adapted from Reference 128 (CC BY 4.0). (*b*) Ti-64 clavicular implant. Image provided by Eng. Gary Muller-Kamskii, Israel Institute of Metals, Technion, Haifa, Israel. (*c*) Co-Cr knee implant. Panel adapted from Reference 128 (CC BY 4.0). (*d*) Ta hip lattice implant. Image provided by Dr. H. P. Tang, State Key Laboratory of Porous Metal Materials, Northwest Institute for Nonferrous Metal Research, Beijing, China. (*e*) Fluorescence F-actin images of bioprinted cardiac cells within a gold nanorod–based bioprinted construct at day 12. Panel adapted from Reference 93 with permission.

PBF-L and PBF-EB, including fatigue characterization (10^6 cycles), and found acceptable levels of strain, stress, and screw-loosening torque. In 2009, Xiu and colleagues (132) developed the first printed titanium spinal implants. Van Bael et al. (133) studied in vitro the effects of pore size and geometry of PBF-L-printed Ti-64 bone scaffolds that use human periosteum-derived cells and concluded that more cells attached to less permeable scaffolds. Hassanin and colleagues (134) reported implants with microchannels for in situ–controlled drug delivery. Recently, Lewin and colleagues (135) compared the mechanical performance of hot-isostatic-pressed (HIPed) PBF-L-printed and PBF-EB-printed mesh-type (features as small as 300 μm) titanium structures for cranial implants. The investigators concluded that the HIPed PBF-L-printed specimens had significantly better mechanical properties and fidelity to the CAD model compared with the PBF-EB-printed specimens; moreover, numerical simulations demonstrated that the geometrical deviation of the PBF-EB-printed parts was the main reason for the striking difference in mechanical performance, although the larger surface roughness of the PBF-EB-printed specimens compared with the HIPed PBF-L-printed specimens also posed a key issue.

4.1.2. Co-Cr alloys. Load-bearing implants (128) and cardiovascular stents (136) have been 3D printed in Co-Cr. In 2012, Murr et al. (128) reported Co-Cr alloy PBF-EB-printed porous knee and hip implants (**Figure 2*c***), minimizing stress shielding and promoting bone growth. Hazlehurst et al. (137) demonstrated PBF-L-printed Co-Cr structures similar to cortical and cancellous femur bone in stiffness and strength. The osseointegration and biomechanical fixation of Co-Cr implants are inferior to those of their titanium counterparts; however, Co-Cr implants coated in calcium aluminate (138) and titanium (139) have shown improved performance.

4.1.3. Tantalum. 3D-printed Ta prosthetics are primarily load-bearing implants (140). AM circumvents the complexity of machining Ta, while mimicking the morphology of the most common Ta-based orthopedic material (Trabecular Metal™—a Ta-coated carbon matrix; see 141), which is used in more than 800,000 acetabular cup surgeries worldwide (140). PBF-L-printed Ta implants show increased bone growth and osseointegration in vivo (142). PBF-L-printed tantalum implants interface well with the bone, enabling continuous load transfer; furthermore, the fatigue limit (10^6 cycles) is 58% of the yield stress, compared with just 12% for Ti-64 scaffolds (140). Bandyopadhyay et al. (143) studied the early-stage osteointegration of DED-L-printed porous implants and concluded that Ta implants provide better cellular attachment and bone interlocking than Ti implants, due to higher surface area and rougher pore topography. In 2020, Tang and colleagues (144) attained a 100% success rate in 27 clinical applications of PBF-EB tantalum bone implants (**Figure 2*d***).

4.1.4. Gold. AM of solid/porous gold implants has not been reported; however, 3D-printed gold nanocomposites have been investigated to create permanent implants that regenerate functional tissue (145). In particular, Zhu and colleagues (93) developed DIW-printable gold nanorod inks for use in cardiac constructs, demonstrating excellent cytocompatibility and improved cell adhesion and organization compared to formulations without gold nanorods (**Figure 2*e***). Their ink creates a proper microenvironment to spread and organize cardiac cells; it also has low viscosity, facilitating high-speed printing without exerting high shear to the encapsulated cells. Further study is required to understand whether the gold nanorods stay in the grown tissue; however, the authors speculate that the gold nanorods are mainly internalized by the cardiac cells after the degradation of the biomaterial matrix, hence becoming permanently implanted in the cardiac tissue (93).

4.2. Biodegradable Implants and Scaffolds

This section surveys the latest reports on additively manufactured, biodegradable metal implants—a relatively new field where some of the key demonstrations were recently attained or are currently pursued; consequently, the field does not have the same degree of development as 3D-printed metal permanent implants. Recent work has focused on the demonstration of tissue scaffolds made of magnesium, iron, and iron-based alloys using various AM methods; characterization of their mechanical properties and cytocompatibility; and tailoring of their degradation rate via engineering of the object's porosity and addition of alloying elements.

4.2.1. Magnesium. Meenashisundaram and colleagues (146) reported a Ti + Mg composite for orthopedic applications where the Ti is BMJ-printed and the Mg is infiltrated; the composite's Young's modulus and ultimate compressive strength match those of human cortical bone. They measured a <1-mm/year corrosion rate in a 0.9% NaCl solution at 37°C and larger osteoblastic cell proliferation for their material than for BMJ-printed porous Ti-only samples. Dutta and colleagues (147) reported that the degradation behavior of porous magnesium is controlled by the pore size, which can be engineered using AM. Kleger and colleagues demonstrated porous magnesium scaffolds via infiltration of DIW-printed salt templates (**Figure 3*a***), showing replication of micrometer-sized features (55). Recently, Kopp and colleagues (148) demonstrated PBF-L-printed Mg scaffolds (**Figure 3*b***), showing that structures with smaller pore size had improved long-term stability, for example, lower hydrogen release.

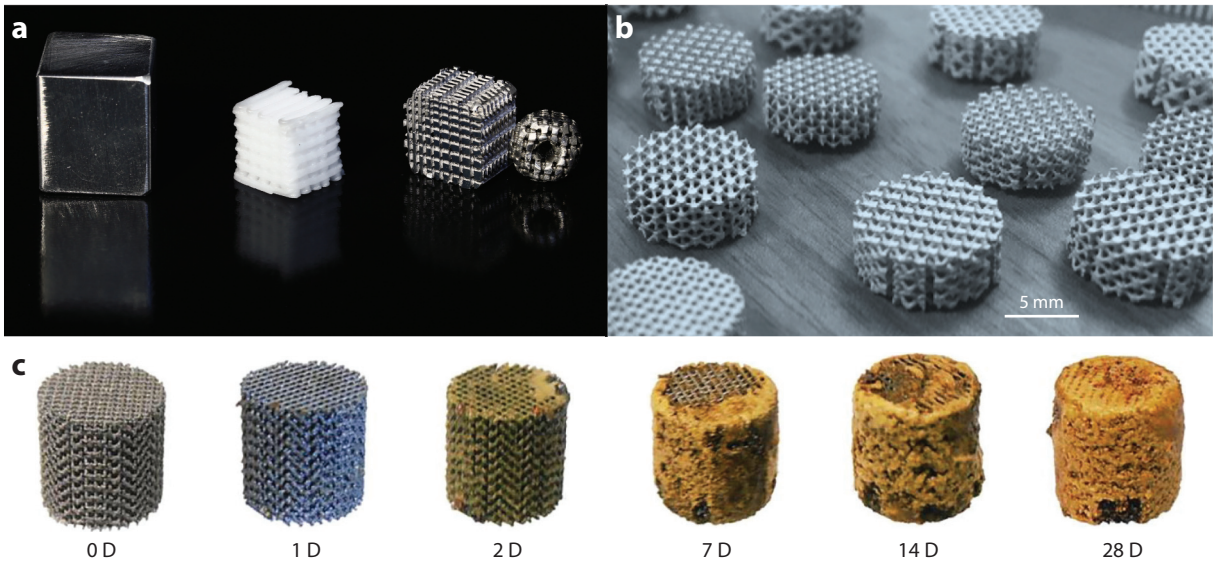

Figure 3

Examples of metal 3D-printed, biodegradable structures. (*a*) From left to right: a solid magnesium cube, a salt template printed by direct ink writing, and two examples of porous magnesium scaffolds made via infiltration of 3D-printed salt templates. Image provided by Complex Materials/Laboratory of Metal Physics and Technology, Department of Materials, ETH Zurich, Zurich, Switzerland. (*b*) An array of PBF-L-printed Mg alloy scaffolds with varying pore size. Image provided by Dr. Alexander Kopp, Meotec GmbH, Aachen, Germany. (*c*) From left to right: in vitro degradation of PBF-L-printed iron scaffolds at 0, 1, 2, 7, 14, and 28 days. Panel adapted from Reference 150 with permission.

4.2.2. Iron. Work on AM biodegradable, iron-based implants has focused on porous structures made of iron and iron-based alloys with Mn, Mg, and Ca as alloying elements. Carluccio and colleagues (149) reported that PBF-L-printed Fe-Mn alloy has a higher degradation rate than that of bulk iron; the higher rate was attributed to the manufacturing method, the addition of Mn, and the design of the scaffold. Hong et al. (84) investigated the effect of adding Ca and Mg on the degradation rate of BMJ-printed specimens made of Fe-Mn alloys. The samples attained porosities as high as 53% and showed a greater corrosion rate than that of sintered, compact samples. In addition, the samples also showed good cytocompatibility with MC3T3 cells. However, the specimens made in Fe-Mn-Ca alloy exhibited higher stiffness and brittle failure than Fe-Mn samples, presumably due to the presence of micropores in the material. Li and colleagues (150) reported PBF-L-printed biodegradable porous iron scaffolds (**Figure 3*c***), with the aim of developing a structure with properties (fully interconnected porous structure, bone-mimicking mechanical properties, and adequate biodegradation profile) suitable for bone regeneration. After 4 weeks of immersion tests, the printed iron specimens showed over a tenfold increase in the biodegradation rate compared with cold-rolled iron, with only 3.1% weight loss, although the elastic modulus and yield strength decreased less than 10%.

4.3. Surgical Tools

AM allows the tailoring of surgical instruments to specific patients, while providing more intuitive ergonomics and better user friendliness to the operator (151). In addition, AM enables the creation of instruments that cannot be made with conventional manufacturing methods; moreover, the low per-unit cost and in situ manufacturing of AM methods could improve healthcare in developing countries (152). Metals are used in surgical devices due to their stiffness, to guide procedures or to apply force to tissue. Metal AM of medical instruments started recently; the US Food and Drug Administration first published guidelines in 2017 (153). There are only dozens of relevant published, peer-reviewed papers on AM of medical instruments; of these, about a tenth report metal devices—often made via PBF (151). The development of surgical tools focuses (~60% of the reports) on SS 316L—which is ideal for temporary interaction with the human body—but some devices made in Ti alloys (~20%) and in Co-Cr alloys (~20%) have also been reported (151).

4.3.1. Titanium alloys. Coemert et al. (154) reported snake-like manipulators for minimally invasive surgery using 3D-printed parts and investigated the replacement of biocompatible polyamide flexural hinges with Ti-64 to further miniaturize their instrument, concluding that electrical discharge machining (a low-throughput, high-precision subtractive method) was more appropriate than PBF. In 2018, Sakes et al. (155) developed a 2-degrees-of-freedom (2-DoF) electrosurgical grasper for minimally invasive surgery, where the Ti-64 tips were PBF-L-printed. Their design produces joints that are stiffer than those of currently available steerable probes; furthermore, their grasper can coagulate tissues, as the jaws are connected to electrode cables (**Figure 4*a***).

4.3.2. Co-Cr alloys. Baila et al. (156) developed a 3D-printed general-purpose dental elevator, with a polymer handle and a beak printed via PBF-L in Co-Cr alloy (**Figure 4*b***); the beak design included holes to lower material costs. The authors reported micrometer-level precision of the beak elements, with enough stiffness to be used to remove ligament from a tooth. In vitro characterization of their devices showed excellent corrosion resistance to artificial saliva.

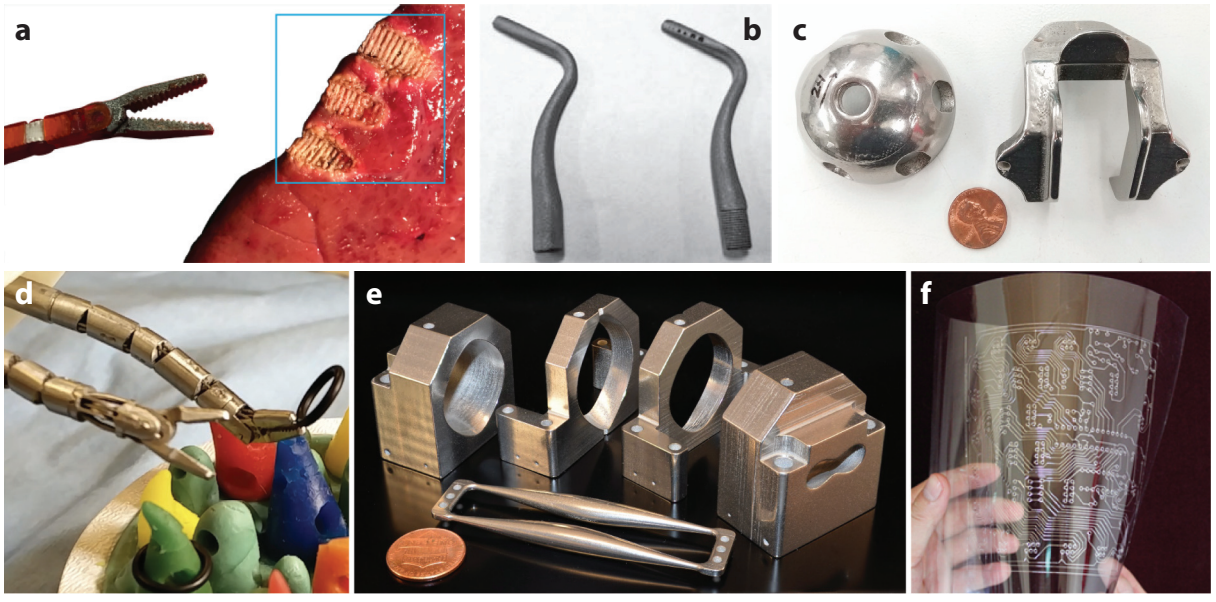

Figure 4

Examples of metal 3D-printed surgical tools and biomedical instrumentation. (*a*) An electrosurgical grasper with PBF-L-printed Ti-64 tips next to a pig liver with several coagulated pieces. Panel adapted from Reference 155 with permission. (*b*) PBF-L-printed beaks part of a dental elevator. Panel adapted from Reference 156 (CC BY 4.0). (*c*) Custom-cut guide and acetabular shell trial PBF-L-printed in SS 316L and polished via vibratory tumbling. Panel adapted from Reference 157 (CC BY-NC-ND 4.0). (*d*) A pair of minimally invasive surgery robotic arms made in SS 316L manipulating an O-ring. Image provided by Professor G.-Z. Yang, Institute of Medical Robotics, Shanghai Jiao Tong University, Shanghai, China. (*e*) Unassembled, miniaturized harmonized multielectrode Kingdon trap made in SS 316L. Panel adapted from Reference 80 with permission. (*f*) A flexible printed circuit board with conductive paths made in Ga alloy. Panel adapted from Reference 164 (CC BY-NC-SA 3.0).

4.3.3. Stainless steel. Nahata & Ozdoganlar (157) reported custom surgical instrumentation for hip and knee implants using PBF-L-printed SS 316L (**Figure 4*c***) and found that (*a*) an iterative printing process can correct for errors in offsets and scaling and (*b*) the AM-fabricated parts retain the mechanical properties of bulk metal, with the exception of the ductility, which was 20–30% lower. Leibrandt and colleagues (158) reported a 7-DoF robot for minimally invasive surgery PBF-L-printed in SS 316L (**Figure 4*d***), concluding that the increased DoFs combined with nonlinear calibration would allow nonexpert operators to perform challenging operations.

4.4. Biomedical Instrumentation

In this section, the latest reports on additively manufactured metal instrumentation are surveyed. Reported devices include mass spectrometry hardware, contrast media for medical imaging, injectable electrodes, and flexible electronics. Metals employed include SS and Ga alloys.

4.4.1. Stainless steel. State-of-the-art chemical analysis uses mass spectrometry (MS), in which ionized samples are sorted by mass-to-charge ratio in high vacuum using electromagnetic fields; however, MS instruments are expensive, bulky, and power hungry, restricting their in situ deployment. Low-cost, compact, analytical-grade chemical sensing could satisfy many exciting Internet of Medical Things applications, such as point-of-care medical diagnostics (159); unfortunately, even after many decades of research, miniaturized MS instruments have orders-of-magnitude

worse performance than standard hardware (160). Arguably, the most important component of a mass spectrometer is the mass filter; fabricating compact mass filters is challenging because of the absolute tolerances required to achieve satisfactory performance. Additionally, the electrode shapes in a mass filter need to be fabricated with high fidelity to generate the fields needed for efficient species sorting. The groups of Velásquez-García at the Massachusetts Institute of Technology and of Nikolaev at Skoltech reported BMJ-printed, fist-sized, harmonized, multielectrode Kingdon traps (electrostatic mass filters based on a harmonic axial field; see **Figure 4*e***) with a 25,000:1 mass resolution (80)—more than two orders of magnitude larger than reported miniaturized mass filters (160), surpassing commercial-grade, nonminiaturized quadrupole-based MS systems.

4.4.2. Gallium alloys. Wang and colleagues (161) investigated injected Ga as a contrast medium for X-ray soft tissue visualization; using ex vivo samples, the investigators showed mega contrast capability in radiological vascular imaging. Analogous mega contrast capability has also been demonstrated with Ga alloys for CT and photoacoustic imaging (162). Jin et al. (163) demonstrated injectable electrodes using a GaInSn alloy, particularly for radiofrequency identification antennas. Zheng and colleagues (164) reported a Ga alloy printer that uses a roller pen with a tapping motion to leave traces of metal as thin as 100 μm on flexible substrates such as polyvinyl chloride and polyethylene terephthalate; capping the prints with a layer of polydimethylsiloxane or silicon rubber stabilizes them. Their technology can be used to make flexible printed circuit boards and antennas for wearable electronics (**Figure 4*f***) (164); Gui et al. (165) obtained similar results by airbrushing a Ga alloy while using a shadow mask for patterning.

5. OUTLOOK

This section describes four exciting, broad opportunities for further development and improvement of metal AM technology with applicability in biomedical engineering: materials, printing technology, artificial intelligence–developed 3D-printed load-bearing implants, and advanced functional implants.

5.1. Materials

Titanium and magnesium alloys were originally developed for the aerospace industry; new formulations, tailored for biomedical applications, are necessary. Better titanium alloys can remove cytotoxic alloy components, such as Al and V, and match human bone in stiffness; possibilities for the latter are using β-type alloys and including engineered porosities in the implant (166). Similarly, magnesium alloys could remove Al and certain rare earth materials to improve biocompatibility or could include essential elements such as Ca, Sr, Zn, and Si to control biodegradation without increasing cytotoxicity (166). Finally, a reformulated SS powder feedstock could increase bioactivity and bone-bonding capability (e.g., SS 316L–hydroxyapatite composites) and improve antibacterial and antimicrobial properties (e.g., SS 316L alloyed with copper) and biocompatibility (e.g., by removing Ni; see 166).

5.2. Printing Technology

Metal AM printing technologies can be improved to better suit biomedical engineering. Potential advances include improving PBF (the most utilized metal AM technology); exploring less commonly used techniques; and using less expensive, capable printing hardware.

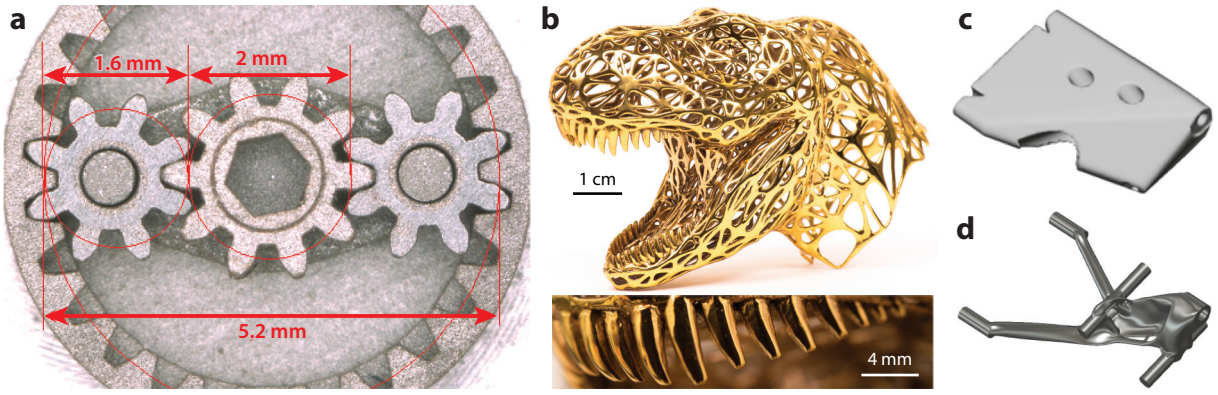

Figure 5

(*a*) A planetary gear made out of tungsten-copper powder via micro-PBF-L. Image provided by Prof. Dr. Horst Exner, Laser Institute Hochschule Mittweida, University of Applied Sciences, Mittweida, Germany. (*b*) 3D Rex, an intricate lost-wax casted metal part made with a wax model via vat polymerization; smallest features are approximately 0.5 mm. Image provided by Octavio Asensio, Octavio Asensio Studio, Madrid, Spain. (*c*) Unoptimized and (*d*) optimized car suspension component using genetic algorithms; the optimized part has constant stresses while minimizing its weight. Images provided by Edgar Cortes-Medina, Tecnologico de Monterrey, Monterrey, Nuevo Leon, Mexico.

AM methods with significantly smaller voxels would be helpful for biomedical purposes; such methods would allow, for example, the definition of finer intricate structures, smaller porous networks, or uniform porous gradients (148). Miniaturized PBF-L was originally developed by the group of Exner (167) using W, Ag, and Cu as feedstock, resulting in 30-μm minimum feature size (**Figure 5*a***). Later, the group of Cullinan (168) demonstrated microscale PBF-L technology that produces Ag parts with voxels that are two orders of magnitude smaller. Their system uses nanoparticle powder as feedstock and a digital light processing chip to structure and project the laser onto the bed of powder; the objects are printed in ∼400-nm layers and have ∼3-μm minimum feature size, with a 63-mm^3/h throughput. The micro-PBF method could enable the creation of fairly complex, miniature metal objects, such as implantable pumps.

Most biomedical metal AM objects are made via PBF, which, with DED, has well-known cyclic thermal issues, particularly for small or finely featured parts (19, 65). However, other commercial-grade, high-resolution metal AM technologies decouple the definition of the object from its solidification into a metal object, which could potentially result in better quality and/or faster manufacturing of biomedical objects. In particular, BMJ is a mature, commercial 3D printing technology with overall better performance than PBF (see Section 3.1.2) that can define ∼35-μm voxels and print titanium, Co-Cr, SS, iron, and magnesium alloys. Further research and development would address current issues with BMJ technology, such as high porosity.

Lost-wax casting (L-WC) is a formative shaping manufacturing method (10), invented at least 6,000 years ago, that creates solid objects. In L-WC, a negative mold is created by casting ceramic around a positive wax model that is then melted out of the mold; afterward, molten material is poured into the mold, forming the desired object, which is then cooled, removed from the mold, and processed to attain a certain surface finish (**Figure 5*b***). L-WC is useful for biomedical applications because it can create intricate parts out of bulk metals such as Au, Ag, SS, and Pt, and even reactive elements such as Mg if L-WC is conducted in vacuum. The wax model can be 3D printed with exquisite detail via BMJ or vat polymerization (19, 65), as is commonly done in the jewelry industry. Models of structures such as porous scaffolds and dental parts could be printed

Lost-wax casting (L-WC): manufacturing method that creates objects by pouring molten material into mold cavities left after melting a wax model

via vat polymerization, and successful casting of such parts can be completed in vacuum (169). Finely featured, mesoscaled sterling silver parts made via L-WC with 3D-printed wax models via vat polymerization showed linearity between the CAD and printed dimensions, average in-plane offset of 40 μm, average out-of-plane offset of 270 μm, and in-plane MFS of 340 μm (80). A negative wax mold was used to print a porous titanium bone-like implant (170).

Ultrasonic additive manufacturing (UAM): manufacturing method that creates objects via ultrasonic scrubbing of metal foils under pressure to cause bonding and periodic cutting of exposed material

Another relatively new manufacturing technology of interest for metal biomedical devices is ultrasonic additive manufacturing (UAM). UAM is a hybrid additive-subtractive process whereby ultrasonic vibrations and pressure induce bonding of metal foils and periodic cutting of the bonded foil stack, typically via milling, to create the desired part geometry (171). Foils used in UAM are typically 10 μm thick. The UAM process was originally invented by Dawn White and patented in 2003 (172); the technology is currently commercialized by Fabrisonic LLC. UAM poses two key advantages over mainstream metal AM methods. First, the foil bonding is in solid phase at temperatures typically below 50% of the metal matrix melting temperature, which makes possible the bonding of dissimilar metals without the formation of a brittle interface as seen in PBF processes (171). Second, UAM has been shown to create multimaterial objects, including metals of biomedical interest such as Au, Fe alloys, Mg alloys, Ti alloys, SS, and Ta (171). There are no examples of biomedical devices made via UAM, but complex objects such as heat exchangers (173) and mechanical and optoelectrical components of interest in biomedical applications—such as optical fibers, magnetostrictive-based sensors, shape-memory-based sensors, and switches—have been successfully embedded in UAM-printed objects (174).

One of the main impediments preventing widespread use of metal AM is the cost of the printing hardware. A typical metal PBF or BMJ printer can cost from several hundreds of thousands to millions of US dollars (2021 prices). Consequently, most metal AM systems are in industrial and academic R&D facilities, operated by highly skilled personnel. However, promising commercialization efforts aim to significantly lower the cost of printing hardware without sacrificing performance, democratizing the technology. For example, the Australian company Aurora Labs (**https://www.auroralabs3d.com**) is commercializing the PBF-L system S-Titanium Pro with a 300-W laser, a 200-mm × 200-mm × 250-mm build envelope, 115-μm in-layer resolution, and 10-μm out-of-layer resolution. The S-Titanium Pro costs less than $90,000, has three independently controlled powder sources, and can print materials of biomedical interest such as SS 316L, CP-Ti, and Ti-64.

5.3. Load-Bearing Implants via Artificial Intelligence

Load-bearing metal implants manufactured via AM can be improved using artificial intelligence. Specifically, genetic algorithms (GAs), that is, robust search algorithms that mimic natural selection by means of biologically inspired operators (e.g., mutation, recombination, and selection according to a fitness function) can be used to optimize the implant. GAs heuristically address the limitations of traditional optimization algorithms, such as the combinatorial increase in complexity when the number of DoFs is increased. To avoid local optimal points, GAs look for solutions in parallel, focusing on the best ones while considering close contenders. In particular, GAs could be used to minimize the weight of an implant while still maintaining load transfer functionality (**Figure 5*c,d***), resulting in significant material cost savings. GAs have recently been used to optimize aneurysm implants using polymer AM (175) and aircraft frames (176).

5.4. Advanced Multifunctional Implants

Excitingly, AM can monolithically create multimaterial, finely featured, multifunctional objects that not only transfer loads but also route signals and actuate, sense, and process information. For

example, using the same printing method, objects with components that are rigid, flexible, conductive, magnetic, and so on could be monolithically integrated to implement complex devices of biomedical interest such as pumps, pacemakers, and drug-delivery microfluidics. Early examples of this vision use polymer printing (16, 17, 177); for metals, any AM method with feedstock directly supplied to the integrating agent (e.g., DED, μPS, FFF, and DIW) can create monolithic, multimaterial objects. In particular, low-temperature processes such as μPS and DIW could be more successful at creating these advanced functional objects, as differential thermal expansion effects would not take place during manufacturing.

SUMMARY POINTS

1. Additive manufacturing (AM)'s attributes, such as print customization, low per-unit cost for small- to mid-batch production, seamless interfacing with mainstream medical 3D imaging techniques, and feasibility to create free-form objects in materials that are biocompatible and biodegradable, are a great fit to a wide range of biomedical applications.
2. The metallic materials most commonly used in biomedical applications are titanium, titanium alloys, Co-Cr alloys, stainless steel, tantalum, gold, magnesium, iron, and gallium alloys; each of these materials can be processed via one or more AM methods.
3. Metal AM techniques encompass (*a*) bulk-supplied powder feedstock selectively joined into a solid object using light, electrons, or binder and (*b*) liquid/paste, filament/wire, or powder feedstock directly fed to the integrating agent (i.e., light, electrons, plasma, heat, or binder) to create a printed object. Historically, metal AM methods with bulk-supplied powder feedstock and a laser or an electron beam as an integrating agent have been more widely used, although other well-established AM methods, such as binder material jetting, with further research and development could yield better, more capable printed objects.
4. The most common biomedical use of 3D-printed metal is permanent and biodegradable load-bearing prosthetic implants, as metals are traditionally used to replace hard tissue. Surgical tools and biomedical instrumentation made via metal AM have also been reported.
5. The different material options available for metal AM result from addressing changes in clinical requirements. Some uses require inertness (e.g., Co-Cr alloys); some require bonding with the host tissue (e.g., titanium, titanium alloys); and some require tissue growth and subsequent implant replacement (e.g., magnesium alloys, iron, and iron alloys).
6. In AM, 3D-printed objects are discretized using voxels that are typically six or more orders of magnitude smaller than the object's volume; consequently, AM can readily create porous structures to avoid stress shielding and to promote tissue growth in implants.
7. Opportunities for further development and improvement of metal AM technology with applicability in biomedical engineering include (*a*) the improvement of mainstream AM methods and associated feedstock; (*b*) the exploration of mature, less utilized metal 3D printing techniques; (*c*) the optimization of load-bearing structures via artificial intelligence; and (*d*) the creation of monolithic, multimaterial, finely featured, multifunctional implants.

DISCLOSURE STATEMENT

The authors are not aware of any affiliations, memberships, funding or financial holdings that may be perceived as affecting the objectivity of this review.

ACKNOWLEDGMENTS

The authors would like to thank Vladimir Popov and Gary Muller-Kamskii, Israel Institute of Metals, Technion, Haifa, Israel; H. P. Tang, State Key Laboratory of Porous Metal Materials, Northwest Institute for Nonferrous Metal Research, Beijing, China; Jörg F. Löffler and the Complex Materials/Laboratory of Metal Physics and Technology, Department of Materials, ETH Zurich, Zurich, Switzerland; Alexander Kopp, Meotec GmbH, Aachen, Germany; Guang-Zhong Yang, Institute of Medical Robotics, Shanghai Jiao Tong University, Shanghai, China; Horst Exner, Laser Institute Hochschule Mittweida, University of Applied Sciences, Mittweida, Germany; Octavio Asensio, Octavio Asensio Studio, Madrid, Spain; and Edgar Cortes-Medina, Tecnologico de Monterrey, Monterrey, Nuevo Leon, Mexico for furnishing some of the images used in this review.

LITERATURE CITED

1. Roser C. 2017. *Faster, Better, Cheaper in the History of Manufacturing: From the Stone Age to Lean Manufacturing and Beyond*. Boca Raton, FL: CRC Press
2. Benvenuto MA. 2016. *Metals and Alloys: Industrial Applications*. Berlin: De Gruyter
3. Worboys M. 2013. Joseph Lister and the performance of antiseptic surgery. *Notes Rec. R. Soc. Lond.* 67(3):199–209
4. Balamurugan A, Rajeswari S, Balossier G, Rebelo AHS, Ferreira JMF. 2008. Corrosion aspects of metallic implants—an overview. *Mater. Corrosion* 59(11):855–69
5. Hlinka J, Kraus M, Hajnys J, Pagac M, Petrů J, et al. 2020. Complex corrosion properties of AISI 316L steel prepared by 3D printing technology for possible implant applications. *Materials* 13(7):1527
6. Pramanik S, Agarwal AK, Rai KN. 2005. Chronology of total hip joint replacement and materials development. *Trends Biomater. Artif. Organs* 19:15–26
7. Rony L, Lancigu R, Hubert L. 2018. Intraosseus metal implants in orthopedics: a review. *Morphologie* 103(339):231–42
8. Geetha M, Singh AK, Asokamani R, Gogia AK. 2009. Ti based biomaterials, the ultimate choice for orthopaedic implants—a review. *Progress Mater. Sci.* 54:397–425
9. Kurtz S, Ong K, Lau E, Mowat F, Halpern M. 2007. Projections of primary and revision hip and knee arthroplasty in the United States from 2005 to 2030. *J. Bone Joint Surg. Am.* 89(4):780–85
10. ASTM Int. 2015. *ISO/ASTM 52900-15, Standard Terminology for Additive Manufacturing—General Principles—Terminology*. West Conshohocken, PA: ASTM Int.
11. Gibson I, Rosen D, Stucker B. 2015. *Additive Manufacturing Technologies: 3D Printing, Rapid Prototyping, and Direct Digital Manufacturing*. New York: Springer. 2nd ed.
12. Ni J, Ling H, Zhang S, Wang Z, Peng Z, et al. 2019. Three-dimensional printing of metals for biomedical applications. *Mater. Today Bio* 3:100024
13. Popov VV, Muller-Kamskii G, Katz-Demyanetz A, Kovalevsky A, Usov S, et al. 2019. Additive manufacturing to veterinary practice: recovery of bony defects after the osteosarcoma resection in canines. *Biomed. Eng. Lett.* 9(1):97–108
14. Waheed S, Cabot J, Macdonald NP, Lewis T, Gujit RM, et al. 2016. 3D printed microfluidic devices: enablers and barriers. *Lab. Chip* 16(11):1993–2013
15. Au AK, Huynh W, Horowitz LF, Folch A. 2016. 3D-printed microfluidics. *Angew. Chem. Int.* 55(12):3862–81
16. Taylor AP, Izquierdo Reyes J, Velásquez-García LF. 2020. Compact, magnetically actuated, additively manufactured pumps for liquids and gases. *J. Phys. D Appl. Phys.* 53(35):355002

17. Taylor AP, Velásquez-García LF. 2017. Miniaturized diaphragm vacuum pump by multi-material additive manufacturing. *J. Microelectromech. Syst.* 26(6):1316–26
18. Melo Máximo D, Velásquez-García LF. 2020. Additively manufactured electrohydrodynamic ionic liquid pure-ion sources for nanosatellite propulsion. *Addit. Manuf.* 36:101719
19. Milewski JO. 2017. *Additive Manufacturing of Metals: From Fundamental Technology to Rocket Nozzles, Medical Implants, and Custom Jewelry*. Cham, Switzerland: Springer
20. Balakrishnan P, Sreekala MS, Thomas S, eds. 2018. *Fundamental Biomaterials: Metals*. Duxford, UK: Woodhead Publishing
21. Henry SD, ed. 2009. *Materials and Coatings for Medical Devices: Cardiovascular*. Materials Park, OH: ASM International
22. Banerjee PC, Al-Saadi S, Choudhary L, Harandi SE, Singh R. 2019. Magnesium implants: prospect and challenges. *Materials* 12(1):136
23. Wu S, Liu X, Yeung KWK, Liu C, Yang X. 2014. Biomimetic porous scaffolds for bone tissue engineering. *Mater. Sci. Eng. R Rep.* 80:1–36
24. Chen Q, Thouas GA. 2015. Metallic implant biomaterials. *Mater. Sci. Eng. R Rep.* 87:1–57
25. Yeganeh VE, Li P. 2017. Effect of beam offset on microstructure and mechanical properties of dissimilar electron beam welded high temperature titanium alloys. *Mater. Des.* 124:78–86
26. Davis JR. 2003. Metallic materials. In *Handbook of Materials for Medical Devices*, ed. JR Davis, pp. 21–50. Materials Park, OH: ASM Int.
27. Lütjering G, Williams JC. 2007. *Titanium*. Leipzig, Germany: Springer
28. Venkatesh BD, Chen DL, Bhole SD. 2009. Effect of heat treatment on mechanical properties of Ti-6Al-4V ELI alloy. *Mater. Sci. Eng. A* 506:117–24
29. Milovanovic A, Sedmak A, Grbovic A, Mijatovic T, Colic K. 2020. Design aspects of hip implant made of Ti-6Al-4V extra low interstitials alloy. *Procedia Struct. Integr.* 26:299–305
30. Khang D, Lu J, Yao C, Haberstroh KM, Webster TJ. 2008. The role of nanometer and sub-micron surface features on vascular and bone cell adhesion on titanium. *Biomaterials* 29:970–83
31. Zhang L-C, Chen L-Y. 2019. A review on biomedical titanium alloys: recent progress and prospect. *Adv. Eng. Mater.* 21:1801215
32. Elias CN, Lima JHC, Valiev R, Meyers MA. 2008. Biomedical applications of titanium and its alloys. *JOM* 60:46–49
33. Bandyopadhyay A, Espana F, Balla VK, Bose S, Ohgami Y, Davies NMJ. 2010. Influence of porosity on mechanical properties and in vivo response of Ti6Al4V implants. *Acta Biomater.* 6(4):1640–48
34. Evans FG. 1976. Mechanical properties and histology of cortical bone from younger and older men. *Anat. Rec.* 185(1):1–11
35. Burstein AH, Reilly DT, Martens M. 1976. Aging of bone tissue: mechanical properties. *J. Bone Joint Surg. Am.* 58(1):82–86
36. Tang JC, Luo JP, Huang YJ, Sun JF, Zhu ZY, et al. 2020. Immunological response triggered by metallic 3D printing powders. *Addit. Manuf.* 22:101392
37. Koutsoukis T, Zinelis S, Eliades G, Al-Wazzan K, Rifaiy MA, Al Jabbari YS. 2015. Selective laser melting technique of Co-Cr dental alloys: a review of structure and properties and comparative analysis with other available techniques. *J. Prosthodont.* 24(4):303–12
38. Kassapidou M, Stenport VF, Hjalmarsson L, Johansson CB. 2017. Cobalt-chromium alloys in fixed prosthodontics in Sweden. *Acta Biomater. Odontol. Scand.* 3(1):53–62
39. Delaunay C, Petit I, Learmonth ID, Oger P, Vendittoli PA. 2010. Metal-on-metal bearings total hip arthroplasty: the cobalt and chromium ions release concern. *Orthop. Traumatol. Surg. Res.* 96(8):894–904
40. Mao X, Wong AA, Crawford RW. 2011. Cobalt toxicity—an emerging clinical problem in patients with metal-on-metal hip prostheses? *Med. J. Aust.* 194:649–51
41. Sahasrabudhe H, Bose S, Bandyopadhyay A. 2018. Laser processed calcium phosphate reinforced CoCrMo for load-bearing applications: processing and wear induced damage evaluation. *Acta Biomater.* 66:118–28
42. Munoz A, Costa M. 2012. Elucidating the mechanisms of nickel compound uptake: a review of particulate and nano-nickel endocytosis and toxicity. *Toxicol. Appl. Pharmacol.* 260:1–16

43. Matthay RA, Balzer PA, Putman CE, Gee JB, Beck GJ, Greenspan RH. 1978. Tantalum oxide, silica and latex: effects on alveolar macrophage viability and lysozyme release. *Investig. Radiol.* 13(6):514–18
44. Rahmati B, Sarhan AD, Zalnezhad E, Kamiab Z, Dabbagh A, et al. 2016. Development of tantalum oxide (Ta-O) thin film coating on biomedical Ti-6Al-4V alloy to enhance mechanical properties and biocompatibility. *Ceramics Int.* 42(1):466–80
45. Wei X, Zhao D, Wang B, Wang W, Kang K, et al. 2016. Tantalum coating of porous carbon scaffold supplemented with autologous bone barrow stromal stem cells for bone regeneration in vitro and in vivo. *Exp. Biol. Med.* 241(6):592–602
46. Demann ETK, Stein PS, Hauberinch JE. 2005. Gold as an implant in medicine and dentistry. *J. Long-Term Effects Med. Implants* 15(6):687–98
47. Gladwin M, Bagby M. 2018. *Clinical Aspects of Dental Materials: Theory, Practice, and Cases*. Philadelphia: Wolters Kluwer. 5th ed.
48. Lansdown ABG. 2018. Gold: Human exposure and update on toxic risks. *Crit. Rev. Toxicol.* 48(7):596–614
49. Hughes MO. 2010. Incorporating gold into ocular prosthetics. *J. Ophthalmic Prosthetics* 15:37–43
50. Wang Y, Wan J, Miron RJ, Zhao Y, Zhang Y. 2016. Antibacterial properties and mechanisms of gold-silver nanocages. *Nanoscale* 8:11143–52
51. Baltzer N, Copponnex T. 2014. Properties and processing of precious metal alloys for biomedical applications. In *Precious Metals for Biomedical Applications*, ed. N Baltzer, T Copponnex, pp. 3–36. Sawston, UK: Elsevier
52. Dykman LA, Khlebtsov NG. 2016. Biomedical applications of multifunctional gold-based nanocomposites. *Biochemistry (Moscow)* 81(13):1771–89
53. Yang Y, He C, Dianyu E, Yang W, Qi F, et al. 2020. Mg bone implant: features, developments and perspectives. *Mater. Des.* 185:108259
54. Zberg B, Uggowitzer PJ, Löffler JF. 2009. MgZnCa glasses without clinically observable hydrogen evolution for biodegradable implants. *Nat. Mater.* 8:887–91
55. Kleger N, Cihova M, Masania K, Studart AR, Löffler JF. 2019. 3D printing of salt as a template for magnesium with structured porosity. *Adv. Mater.* 31:1903783
56. Liu J, Yi L. 2018. *Liquid Metal Biomaterials—Principles and Applications*. Singapore: Springer
57. Yi L, Liu J. 2017. Liquid metal biomaterials: a newly emerging area to tackle modern biomedical challenges. *Int. Mater. Rev.* 62(7):415–40
58. Yan J, Lu Y, Chen G, Yang M, Gu Z. 2018. Advances in liquid metals for biomedical applications. *Chem. Soc. Rev.* 47:21518
59. Scharmann F, Cherkashinin G, Breternitz V, Knedlik C, Hartung G, et al. 2004. Viscosity effect on GaInSn studied by XPS. *Surf. Interface Anal.* 36(8):981–85
60. Liu F, Yu Y, Yi L, Liu J. 2016. Liquid metal as reconnection agent for peripheral nerve injury. *Sci. Bull.* 61(12):939–47
61. Wang X, Liu J. 2016. Recent advancements in liquid metal flexible printed electronics: properties, technologies, and applications. *Micromachines* 7(12):206
62. Palleau E, Reece S, Desai SC, Smith ME, Dickey MD. 2013. Self-healing stretchable wires for reconfigurable circuit wiring and 3D microfluidics. *Adv. Mater.* 25:1589–92
63. Li Y, Jahr H, Zhou J, Zadpoor AA. 2020. Additively manufactured biodegradable porous metals. *Acta Biomater.* 115:29–50
64. Kraus T, Moszner F, Fischerauer S, Fiedler M, Martinelli E, et al. 2014. Biodegradable Fe-based alloys for use in osteosynthesis: outcome of an in vivo study after 52 weeks. *Acta Biomater.* 10(7):3346–53
65. Bar-Cohen Y, ed. 2018. *Advances in Manufacturing and Processing of Materials and Structures*. Boca Raton, FL: CRC Press
66. Ghods S, Schultz E, Wisdom C, Schur R, Pahuja R, et al. 2020. Electron beam additive manufacturing of Ti6Al4V: evolution of powder morphology and part microstructure with powder reuse. *Materialia* 9:100631
67. Jianzhong R, Sparks TE, Fan Z, Stroble JK, Panackal A. 2006. A review of layer based manufacturing processes for metals. In *2006 International Solid Freeform Fabrication Symposium*, pp. 233–45. Austin: Univ. Tex. Press

68. Srivastava M, Rathee S, Maheshwari S, Kundra TK. 2019. *Additive Manufacturing: Fundamentals and Advancements*. Boca Raton, FL: CRC Press
69. Mower TM, Long MJ. 2016. Mechanical behavior of additive manufactured, powder-bed laser-fused materials. *Mater. Sci. Eng. A* 651:198–213
70. Frazier WE. 2014. Metal additive manufacturing: a review. *J. Mater. Eng. Perform.* 23(6):1917–28
71. Yadroitsev I, Krakhmalev P, Yadroitsava I, Johansson S, Smurov I. 2013. Energy input effect on morphology and microstructure of selective laser melting single track from metallic powder. *J. Mater. Process. Technol.* 213(4):606–13
72. Abd-Elghany K, Bourell DL. 2012. Property evaluation of 304L stainless steel fabricated by selective laser melting. *Rapid Prototyp. J.* 18(3):420–28
73. Sachdeva A, Singh S, Sharma VS. 2013. Investigating surface roughness of parts produced by SLS process. *Int. J. Adv. Manuf. Technol.* 64:1505–16
74. Murr LE, Martinez E, Hernandez J, Collins S, Amato KN, et al. 2012. Microstructures and properties of 17-4 PH stainless steel fabricated by selective laser melting. *J. Mater. Res. Technol.* 1(3):167–77
75. General Electric. 2021. *Inside electron beam melting*. White Pap., General Electric, Boston. **https://go.additive.ge.com/rs/706-JIU-273/images/GE%20Additive_EBM_White%20paper_FINAL.pdf**
76. Kumar S. 2020. *Additive Manufacturing Processes*. Cham, Switz.: Springer
77. Wysocki B, Maj P, Sitek R, Buhagiar J, Kurzydłowski KJ, Święszkowski W. 2017. Laser and electron beam additive manufacturing methods of fabricating titanium bone implants. *Appl. Sci.* 7(7):657
78. Sames WJ, List FA, Pannala S, Dehoff RR, Babu SS. 2016. The metallurgy and processing science of metal additive manufacturing. *Int. Mater. Rev.* 61(5):315–60
79. Mirzababaei S, Pasebani S. 2019. A review of binder jet additive manufacturing of 316L stainless steel. *J. Manuf. Mater. Process.* 3(3):82
80. Sun Z, Vladimirov G, Nikolaev E, Velásquez-García LF. 2018. Exploration of metal 3-D printing technologies for the microfabrication of freeform, finely featured, mesoscaled structures. *J. Microelectromech. Syst.* 27(6):1171–85
81. Verlee B, Dormal T, Lecomte-Beckers J. 2012. Density and porosity control of sintered 316L stainless steel parts produced by additive manufacturing. *Powder Metall.* 55(4):260–67
82. ExOne. 2020. Metal 3D printers—materials & binders. *ExOne*. **https://www.exone.com/en-US/3d-printing-materials-and-binders/metal-materials-binders**
83. Salehi M, Maleksaeedi S, Sapari MAB, Nai MLS, Meenashisundaram GK, Gupta M. 2019. Additive manufacturing of magnesium-zin-zirconium (ZK) alloys via capillary-mediated binderless three-dimensional printing. *Mater. Des.* 169:107683
84. Hong D, Chou D-T, Velikokhatnyi OI, Roy A, Lee B, et al. 2016. Binder-jetting 3D printing and alloy development of new biodegradable Fe-Mn-Ca/Mg alloys. *Acta Biomater.* 45:375–86
85. Davé V. 1995. *Electron beam (EB)-assisted materials fabrication*. PhD Thesis, Mass. Inst. Technol., Cambridge, MA
86. Taminger KM, Watson JK, Hafley RA, Petersen DD. 2003. *Solid freeform fabrication apparatus and methods*. US Patent 7,168,935
87. Wholers T, Gornet T. 2014. History of additive manufacturing. *Wholers Report*. **http://wohlersassociates.com/history2014.pdf**
88. BASF. 2020. Ultrafuse® 316L: Stainless steel composite metal filament for 3D printers. *BASF Group*. **https://www.forward-am.net/find-material/filaments/ultrafuse-316l/**
89. Wolff M, Mesterknecht T, Bals A, Ebel T, Willumeit-Römer R. 2019. FFF of Mg-alloys for biomedical application. In *Magnesium Technology 2019*, ed. VV Joshi, JB Jordon, D Orlov, NR Neelameggham, pp. 43–49. Cham, Switzerland: Springer
90. Wolff M, Schaper JG, Dahms M, Ebel T, Kainer KU, Klassen T. 2014. Magnesium powder injection moulding for biomedical application. *Powder Metall.* 57(5):331–40
91. Lewis J. 2016. Direct ink writing of 3D functional materials. *Adv. Funct. Mater.* 16(17):2193–204
92. Hirt L, Reiser A, Spolenak R, Zambelli T. 2017. Additive manufacturing of metal structures at the micrometer scale. *Adv. Mater.* 29:1604211
93. Zhu K, Shin SR, van Kempen T, Li Y-C, Ponraj V, et al. 2017. Gold nanocomposite bioink for printing 3D cardiac constructs. *Adv. Funct. Mater.* 27:1605352

94. Zhang J, Zhao S, Zhu M, Zhu Y, Zhang Y, et al. 2014. 3D-printed magnetic Fe3O4/MBG/PCL composite scaffolds with multifunctionality of bone regeneration, local anticancer drug delivery and hyperthermia. *J. Mater. Chem.* 2(43):7583–95
95. Hoshino K, Morikawa M, Kohno T, Ueda K, Miyakawa M. 1994. *Moldable mixture for use in the manufacturing of precious metal articles*. US Patent 5,328,775
96. Hartkop DT. 2016. *Build Your Own Mini Metal Maker: 3D Print with Metal Clay, Ceramic, Chocolate, Stem Cells, or Whatever!* Scotts Valley, CA: CreateSpace Independent Publishing Platform
97. Segura-Cárdenas E, Velásquez-García LF. 2020. Additively manufactured robust microfluidics via silver clay extrusion. *J. Microelectromech. Syst.* 29(3):427–37
98. Campbell SA. 2013. *Fabrication Engineering and the Micro- and Nanoscale*. New York: Oxford Univ. Press
99. Burwell ED. 2015. *A microplasma-based sputtering system for direct-write, microscale fabrication of thin-film metal structures*. MS Thesis, Case Western Reserve University, Cleveland, OH
100. Abdul-Wahed AM, Roy AL, Xiao Z, Takahata K. 2018. Direct writing of metal film via sputtering of micromachined electrodes. *J. Mater. Process. Technol.* 262:403–10
101. Wang T, Lv L, Shi L, Tong B, Zhang X, et al. 2020. Microplasma direct writing of a copper thin film in the atmospheric condition with a novel copper powder electrode. *Plasma Process. Polymers* 17:e2000034
102. Guo QJ, Ni GH, Li L, Lin QF, Zhao YJ, et al. 2018. Effects of input power, gas flow rate and hydrogen concentration on Cu film deposition by a radio frequency driven non-thermal atmospheric pressure plasma jet. *Thin. Solid Films* 660:493–98
103. Kornbluth YS, Mathews RH, Parameswaran L, Racz LM, Velásquez-García LF. 2018. Microsputterer with integrated ion-drag focusing for additive manufacturing of thin, narrow conductive lines. *J. Phys. D Appl. Phys.* 51(16):165603
104. Kornbluth YS, Mathews RH, Parameswaran L, Racz LM, Velásquez-García LF. 2019. Room-temperature, atmospheric-pressure microsputtering of dense, electrically conductive, sub-100 nm gold films. *Nanotechnology* 30(28):285602
105. Kornbluth YS, Mathews RH, Parameswaran L, Racz LM, Velásquez-García LF. 2019. Room-temperature printing of micron-scale-wide metal lines for microsystems via atmospheric microsputtering. In *Technical Digest 32nd Conference on Micro Electro Mechanical Systems* (*MEMS 2019*), ed. S Takeuchi, JB Yoon, pp. 372–75. Piscataway, NJ: IEEE
106. Lyu H, Zhang X, Liu F, Huang Y, Zhang Z, et al. 2019. Fabrication of micro-scale radiation shielding structures using tungsten nanoink through electrohydrodynamic jet printing. *J. Micromech. Microeng.* 29(11):115004
107. Samarasinghe SR, Pastoriza-Santos I, Edirisinghe MJ, Liz-Marzán LM. 2008. Fabrication of nanostructured gold films by electrohydrodynamic atomization. *Appl. Phys. A* 91:141–47
108. Lee MW, An S, Kim NY, Seo JH, Huh J-Y, et al. 2013. Effects of pulsing frequency on characteristics of electrohydrodynamic inkjet using micro-Al and nano-Ag particles. *Exp. Therm. Fluid Sci.* 46:103–10
109. Matsuura T, Takai T, Iwata F. 2017. Local electrophoresis deposition assisted by laser trapping coupled with a spatial light modulator for three-dimensional microfabrication. *Jpn. J. Appl. Phys.* 56(10):105502
110. Zenou M, Sa'ar A, Kotler Z. 2015. Laser transfer of metals and metal alloys for digital microfabrication of 3D objects. *Small* 11(33):4082–89
111. Feinaeugle M, Pohl R, Bor T, Vaneker T, Römer G-W. 2018. Printing of complex free-standing microstructures via laser-induced forward transfer (LIFT) of pure metal thin films. *Addit. Manuf.* 24:391–99
112. Hu J, Yu M-F. 2010. Meniscus-confined three-dimensional electrodeposition for direct writing of wire bonds. *Science* 329(5989):313–16
113. Zhang X, Zhang Y, Li Y, Lei Y, Li Z, et al. 2019. Bipolar electrochemistry regulation for dynamic meniscus confined electrodeposition of copper micro-structures by a double-anode system. *J. Electrochem. Soc.* 166(13):D676
114. Tanaka T, Ishikawa A, Kawata S. 2006. Two-photon-induced reduction of metal ions for fabricating three-dimensional electrically conductive metallic microstructure. *Appl. Phys. Lett.* 88(8):081107
115. Barton P, Mukherjee S, Prabha J, Boudouris BW, Pan L, Xu X. 2017. Fabrication of silver nanostructures using femtosecond laser-induced photoreduction. *Nanotechnology* 28(50):505302

116. Li C, Hu J, Jiang L, Xu C, Li X, et al. 2020. Shaped femtosecond laser induced photoreduction for highly controllable Au nanoparticles based on localized field enhancement and their SERS applications. *Nanophotonics* 9(3):691–702
117. Henry MR, Kim S, Fedorov AG. 2016. High purity tungsten nanostructures via focused electron beam induced deposition with carrier gas assisted supersonic jet delivery of organometallic precursors. *J. Phys. Chem. C* 120(19):10584–90
118. Córdoba R, Orús P, Strohauer S, Torres TE, De Teresa JM. 2019. Ultra-fast direct growth of metallic micro- and nano-structures by focused ion beam irradiation. *Sci. Rep.* 9:14076
119. Kornbluth Y, Mathews RH, Parameswaran L, Racz L, Velásquez-García LF. 2020. Nano-additively manufactured gold thin films with high adhesion and near-bulk electrical resistivity via jet-assisted, nanoparticle-dominated, room-temperature microsputtering. *Addit. Manuf.* 36:101679
120. Jamieson R, Holmer B, Ashby A. 1995. How rapid prototyping can assist in the development of new orthopaedic products: a case study. *Rapid Prototyp. J.* 1:38–41
121. Kim J-H, Kim M-Y, Knowles JC, Choi S, Kang H, et al. 2020. Mechanophysical and biological properties of a 3D-printed titanium alloy for dental applications. *Dental Mater.* 36(7):945–58
121a. Lee U-L, Kwon J-S, Woo S-H, Choi Y-J. 2016. Simultaneous bimaxillary surgery and mandibular reconstruction with a 3-dimensional printed titanium implant fabricated by electron beam melting: a preliminary mechanical testing of the printed mandible. *J. Oral Maxillofac. Surg.* 74(7):1501.e1–15
122. Park E-K, Lim J-Y, Yun I-S, Kim J-S, Woo S-H, et al. 2016. Cranioplasty enhanced by three-dimensional printing: custom-made three-dimensional-printed titanium implants for skull defects. *J. Craniofac. Surg.* 27(4):943–49
123. Imanishi J, Choong PFM. 2015. Three dimensional printed calcaneal prosthesis following total calcanectomy. *Int. J. Surg. Case Rep.* 10:83–87
124. Aranda JL, Jiménez MF, Rodríguez M, Varela G. 2015. Tridimensional titanium-printed custom-made prosthesis for sternocostal reconstruction. *Eur. J. Cardiothorac. Surg.* 48(4):e92–94
125. Mobbs RJ, Coughlan M, Thompson R, Sutterlin CE, Phan K. 2017. The utility of 3D printing for surgical planning and patient-specific implant design for complex spinal pathologies: case report. *J. Neurosurg. Spine* 26(4):513–18
126. Hsu RA, Ellington JK. 2015. Patient-specific 3-dimensional printed titanium truss cage with tibiotalocalcaneal arthrodesis for salvage of persistent distal tibia nonunion. *Foot Ankle Spec.* 8(6):483–89
127. Dekker TJ, Steele JR, Federer AE, Hamid KS, Adams SB. 2018. Use of patient-specific 3D-printed titanium implants for complex foot and ankle limb salvage, deformity correction, and arthrodesis procedures. *Foot Ankle Int.* 39(8):916–21
128. Murr LE, Gaytan SM, Martinez E, Medina F, Wicker RBJ. 2012. Next generation orthopaedic implants by additive manufacturing using electron beam melting. *Int. J. Biomater.* 2012:245727
129. Mangano C, Bianchi A, Mangano FG, Dana J, Colombo M, et al. 2020. Custom-made 3D printed subperiosteal titanium implants for the prosthetic restoration of the atrophic posterior mandible of elderly patients: a case series. *3D Print. Med.* 6:1
130. Popov VV Jr., Muller-Kamskii G, Kovalevsky A, Dzhenzhera G, Strokin E, et al. 2018. Design and 3D-printing of titanium bone implants: brief review of approach and clinical cases. *Biomed. Eng. Lett.* 8(4):337–44
131. Barbin T, Velôso DV, Del Rio Silva L, Borges GA, Camacho Presotto AG, et al. 2020. 3D metal printing in dentistry: an in vitro biomechanical comparative study of two additive manufacturing technologies for full-arch implant-supported prostheses. *J. Mech. Behav. Biomed. Mater.* 108:103821
132. Xiu P, Jia Z, Lv J, Yin C, Cheng Y, et al. 2016. Tailored surface treatment of 3D printed porous Ti6Al4V by microarc oxidation for enhanced osseointegration via optimized bone in-growth patterns and interlocked bone/implant interface. *ACS Appl. Mater. Interfaces* 8(28):17964–75
133. Van Bael S, Chai YC, Truscello S, Moesen M, Kerckhofs G, et al. 2012. The effect of pore geometry on the in vitro biological behavior of human periosteum-derived cells seeded on selective laser-melted Ti6Al4V bone scaffolds. *Acta Biomater.* 8(7):2824–34
134. Hassanin H, Finet L, Cox SC, Jamshidi P, Grover LM, et al. 2018. Tailoring selective laser melting process for titanium drug-delivering implants with releasing micro-channels. *Addit. Manuf.* 20:144–55

135. Lewin S, Fleps I, Åberg J, Ferguson SJ, Engqvist H, et al. 2021. Additively manufactured mesh-type titanium structures for cranial implants: E-PBF vs. L-PBF. *Mater. Design* 197:109207
136. Finazzi V, Demir AG, Biffi CA, Migliavacca F, Petrini L, Previtali B. 2020. Design and functional testing of a novel balloon-expandable cardiovascular stent in CoCr ally produced by selective laser melting. *J. Manuf. Process.* 55:161–73
137. Hazlehurst K, Wang CJ, Stanford M. 2013. Evaluation of the stiffness characteristics of square pore CoCrMo cellular structures manufactured using laser melting technology for potential orthopaedic applications. *Mater. Des.* 51:949–55
138. Shah FA, Omar O, Suska F, Snis A, Matic A, et al. 2016. Long-term osseointegration of 3D printed CoCr constructs with an interconnected open-pore architecture prepared by electron beam melting. *Acta Biomater.* 36:296–309
139. Kim SC, Jo WL, Kim YS, Kwon SY, Cho YS, Lim YW. 2019. Titanium powder coating using metal 3D printing: a novel coating technology for cobalt-chromium alloy implants. *Tissue Eng. Regen. Med.* 16:11–18
140. Wauthle R, van der Stok J, Yavari SA, Van Humbeeck J, Kruth J-P, et al. 2015. Additively manufactured porous tantalum implants. *Acta Biomater.* 14:217–25
141. Bobyn JD, Stackpool GJ, Hacking SA, Tanzer M, Krygier JJ. 1999. Characteristics of bone ingrowth and interface mechanics of a new porous tantalum biomaterial. *J. Bone Joint Surg. Br.* 81:907–14
142. Guo Y, Xie K, Jiang W, Wang L, Li G, et al. 2019. In vitro and in vivo study of 3D-printed porous tantalum scaffolds for repairing bone defects. *ACS Biomater. Sci. Eng.* 5(2):1123–33
143. Bandyopadhyay A, Mitra I, Shivaram A, Dasgupta N, Bose S. 2019. Direct comparison of additively manufactured porous titanium and tantalum implants towards in vivo osseointegration. *Addit. Manuf.* 28:259–66
144. Tang HP, Yang K, Jia L, He WW, Yang L, Zhang XZ. 2020. Tantalum bone implants printed by selective electron beam manufacturing (SEBM) and their clinical applications. *JOM* 72:1016–21
145. Skardal A, Zhang J, McCoard L, Oottamasathien S, Prestwich GD. 2010. Dynamically crosslinked gold nanoparticle–hyaluronan hydrogels. *Adv. Mater.* 22:4736–40
146. Meenashisundaram GK, Wang N, Maskomani S, Lu S, Anantharajan SK, et al. 2020. Fabrication of Ti + Mg composites by three-dimensional printing of porous Ti and subsequent pressureless infiltration of biodegradable Mg. *Mater. Sci. Eng. C* 108:110478
147. Dutta S, Devi KB, Roy M. 2017. Processing and degradation behavior of porous magnesium scaffold for biomedical applications. *Adv. Powder Technol.* 28:3204–12
148. Kopp A, Derra T, Müther M, Jauer L, Schleifenbaum JH, et al. 2019. Influence of design and postprocessing parameters on the degradation behavior and mechanical properties of additively manufactured magnesium scaffolds. *Acta Biomater.* 98:23–35
149. Carluccio D, Xu C, Venezuela J, Cao Y, Kent D, et al. 2020. Additively manufactured iron-manganese for biodegradable porous load-bearing bone scaffold applications. *Acta Biomater.* 103:346–60
150. Li Y, Jahr H, Lietaert K, Pavanram P, Yilmaz A, et al. 2018. Additively manufactured biodegradable porous iron. *Acta Biomater.* 77:380–93
151. Culmone C, Smit G, Breedveld P. 2019. Additive manufacturing of medical instruments: a state-of-the-art review. *Addit. Manuf.* 27:461–73
152. Ibrahim AMS, Jose RR, Rabie AM, Gerstle TL, Lee BT, Lin SJ. 2015. Three-dimensional printing in developing countries. *Plast. Reconstr. Surg. Glob. Open* 3:e443
153. US Food Drug Admin. 2017. *Technical considerations for additive manufactured medical devices*. FDA-2016-D-1210, US Food Drug Admin., Rockville, MD. **https://www.fda.gov/regulatory-information/search-fda-guidance-documents/technical-considerations-additive-manufactured-medical-devices**
154. Coemert S, Traeger MF, Graf EC, Lueth TC. 2017. Suitability evaluation of various manufacturing technologies for the development of surgical snake-like manipulators from metals based on flexure hinges. *Procedia CIRP* 65:1–6
155. Sakes A, Hovlan K, Smit G, Geraedts J, Breedveld P. 2018. Design of a novel three-dimensional-printed two degrees-of-freedom steerable electrosurgical grasper for minimally invasive surgery. *J. Med. Devices* 12(1):011007

156. Baila DI, Doicin CV, Cotrut CM, Ulmeanu ME, Ghionea IG, Tarba CI. 2016. Sintering the beaks of the elevator manufactured by direct metal laser sintering (DMSL) process from Co-Cr alloy. *Metalurgija* 55(4):663–66
157. Nahata S, Ozdoganlar OB. 2019. Feasibility of metal additive manufacturing for fabricating custom surgical instrumentation for hip and knee implants. *Procedia Manuf.* 34:772–79
158. Leibrandt K, Wisanuvej P, Gras G, Shang J, Seneci CA, et al. 2017. Effective manipulation in confined spaces of highly articulated robotic instruments for single access surgery. *IEEE Robot. Autom. Lett.* 2(3):1704–11
159. Banerjee S. 2020. Empowering clinical diagnostics with mass spectrometry. *ACS Omega* 5(5):2041–48
160. Snyder DT, Pulliam CJ, Ouyang Z, Cooks RG. 2016. Miniature and fieldable mass spectrometers: recent advances. *Anal. Chem.* 88(1):2–29
161. Wang Q, Yu Y, Pan K, Liu J. 2014. Liquid metal angiography for mega contrast X-ray visualization of vascular network in reconstructing in-vitro organ anatomy. *IEEE Trans. Biomed. Eng.* 61(7):2161–66
162. Yan J, Lu Y, Chen G, Yang M, Gu Z. 2018. Advances in liquid metals for biomedical applications. *Chem. Soc. Rev.* 47:2518–33
163. Jin C, Zhang J, Li X, Yang X, Li J, Liu J. 2013. Injectable 3D fabrication of medical electronics at the target biological tissues. *Sci. Rep.* 3:3442
164. Zheng Y, He Z-Z, Yang J, Liu J. 2015. Personal electronics printing via tapping mode composite liquid metal ink delivery and adhesion mechanism. *Sci. Rep.* 4:4588
165. Gui H, Tan SC, Wang Q, Yu Y, Liu FJ, et al. 2017. Spraying printing of liquid metal electronics on various clothes to compose wearable functional device. *Sci. China Technol. Sci.* 60:306–16
166. Vanmeensel K, Lietaert K, Vrancken B, Dadbakhsh S, Li X, et al. 2018. Additively manufactured metals for medical applications. In *Additive Manufacturing—Materials Processes, Quantifications and Applications*, ed. J Zhang, Y-G Jung, pp. 261–309. Oxford, UK: Elsevier
167. Regenfuss P, Hartwig L, Klötzer S, Ebert R, Exner H. 2003. Microparts by a novel modification of selective laser sintering. In *Proceedings of Rapid Prototyping and Manufacturing Conference*, pp. 1–7. Southfield, MI: SME
168. Roy NK, Behera D, Dibua OG, Foong CS, Cullinan MA. 2018. Single shot, large area metal sintering with micrometer level resolution. *Opt. Express* 26(20):25534–44
169. Baltes H, Brand O, Fedder GK, Hierold C, Korvink JG, Tabata O, eds. 2005. *Microengineering of Metals and Ceramics: Part II: Special Replication Techniques, Automation, and Properties*. Darmstadt, Germany: Wiley-VCH
170. Ryan GE, Pandit AS, Apatsidis DP. 2008. Porous titanium scaffolds fabricated using a rapid prototyping and powder metallurgy technique. *Biomaterials* 29(27):3625–35
171. Vaezi M, Drescher P, Seitz H. 2020. Beamless metal additive manufacturing. *Materials* 13(4):922
172. White D. 2003. *Ultrasonic object consolidation*. US Patent 6,519,500
173. Norfolk M, Johnson H. 2015. Solid-state additive manufacturing for heat exchangers. *JOM* 67:655–59
174. Bournias-Varotsis A, Han X, Harris RA, Engstrom DS. 2019. Ultrasonic additive manufacturing using feedstock with build-in circuitry for 3D metal embedded electronics. *Addit. Manuf.* 29:100799
175. Jiang L, Chen S, Sadasivan C, Jiao X. 2017. Structural topology optimization for generative design of personalized aneurysm implants: design, additive manufacturing, and experimental validation. In *Proceedings 2017 IEEE Healthcare Innovation Point Care Technologies* (*HI-POCT 2017*), ed. A Dhawan, G Mensah, pp. 9–13. Piscataway, NJ: IEEE
176. Skinner SN, Zare-Behtash H. 2018. State-of-the-art in aerodynamic shape optimization methods. *Appl. Soft Comput.* 62:933–62
177. Li F, Macdonald NP, Guijt RM, Breadmore MC. 2019. Increasing the functionalities of 3D printed microchemical devices by single material, multimaterial, and print-pause-print 3D printing. *Lab. Chip* 19:35–49

RELATED RESOURCES

Qin Y, Wen P, Guo H, Xia D, Zheng Y, et al. 2019. Additive manufacturing of biodegradable metals: current research status and future perspectives. *Acta Biomater*. 98:3–22

Revilla-León M, Meyer MJ, Özcan M. 2019. Metal additive manufacturing technologies: literature review of current status and prosthodontic applications. *Int. J. Comput. Dent*. 22(1):55–67

Wen P, Voshage M, Jauer L, Chen Y, Qin Y, et al. 2018. Laser additive manufacturing of Zn metal parts for biodegradable applications: processing, formation quality and mechanical properties. *Mater. Des*. 155:36–45

Chou DT, Wells D, Hong D, Lee B, Kuhn H, Kumta PN. 2013. Novel processing of iron–manganese alloy-based biomaterials by inkjet 3-D printing. *Acta Biomater.* 9(10):8593–603

Demir AG, Monguzzi L, Previtali B. 2017. Selective laser melting of pure Zn with high density for biodegradable implant manufacturing. *Addit. Manuf.* 15:20–28

Wen P, Voshage M, Jauer L, Chen Y, Qin Y, et al. 2018. Laser additive manufacturing of Zn metal parts for biodegradable applications: processing, formation quality and mechanical properties. *Mater. Des.* 155:36–45

Liu F, Alici G, Zhang B, Beirne S, Li W. 2015. Structures, fabrication and characterization of a magnetic microactuator based on deformable Fe-doped PDMS artificial cilium using 3D printing. *Smart Mater. Struct.* 24(3):035015

Taylor AP, Vélez Cuervo C, Arnold D, Velásquez-García LF. 2019. Fully 3D-printed, monolithic magnetic actuators for low-cost, compact systems. *J. Microelectromech. Syst.* 28(3):481–93

Sun Z, Velásquez-García LF. 2020. Miniature, metal 3D-printed, multiplexed electrohydrodynamic gas pumps. *Plasma Res. Express* 2(2):025009